



Petrogenesis of the early Paleozoic strongly peraluminous granites in the Western South China Block and its tectonic implications

Touping Peng ^{a,b,*}, Weiming Fan ^{b,c}, Guochun Zhao ^d, Bingxia Peng ^a, Xiaoping Xia ^a, Yongsheng Mao ^{a,e}

^a State Key Laboratory of Isotope Geochemistry, Guangzhou Institute of Geochemistry, Chinese Academy of Sciences, Guangzhou 510640, China

^b CAS Center for Excellence in Tibetan Plateau Earth Sciences, Beijing 100101, China

^c Institute of Tibetan Plateau Research, Chinese Academy of Sciences, Beijing 100101, China

^d Department of Earth Sciences, The University of Hong Kong, Pokfulam Road, Hong Kong

^e Graduate University of Chinese Academy of Sciences, Beijing 100049, China



ARTICLE INFO

Article history:

Received 9 August 2014

Received in revised form 11 November 2014

Accepted 27 November 2014

Available online 4 December 2014

Keywords:

Dulong batholith

Strongly peraluminous granite

Early Paleozoic

Magma mixing

South China Block

ABSTRACT

Strongly peraluminous (SP) granites have A/CNK (molecular $\text{Al}_2\text{O}_3/(\text{CaO}+\text{Na}_2\text{O}+\text{K}_2\text{O})$) ratios >1.1 , indicating a predominant origin from the partial melting of metasedimentary rocks. However, an increasing number of studies have documented that mantle-derived magmas can also be involved in the petrogenesis of some SP granites. This is the case in the Dulong batholith in the southeastern Yunnan province, southwestern South China Block, which is typically composed of SP granitic rocks with high A/CNK values (>1.1). Zircon U-Pb dating of four samples from this batholith yielded consistent crystallization ages of ca. 430 Ma, synchronous with the widespread late-orogenic magmatism (including S- and I-type granites and mafic igneous rocks) in the Wuyi-Yunkai orogen, South China Block (SCB). All the granites have fractionated REE patterns ($(\text{La}/\text{Yb})_{\text{N}} = 1.28\text{--}12.3$) and conspicuous negative Eu anomalies ($\text{Eu}^*/\text{Eu} = 0.07\text{--}0.43$) with a similar depletion in HFSE (Nb, Zr, Hf), P, Ba and Sr, suggesting that these granitic magmas had a dominantly crustal source, likely the Neoproterozoic metasedimentary rocks (i.e., the Danzhou or Banxi groups) that are dominated by pelitic rocks with minor interlayered siltstones in the western Yangtze Block. However, their zircon Hf isotopic results also reveal an important input of the mantle-derived melts into their parental magma. Taken together, their geochemical and isotopic compositions reflect a derivation by magma mixing between the crust- and mantle-derived ($\sim 10\%$ in volume) magmas. Their chemical variations resulted from the fractionation process during the emplacement from the magma chamber after magmatic mixing.

In conjunction with regional data within the SCB, it is most likely that the magmatism younger than 435 Ma was generated in a post-collisional extensional regime related to the partial delamination of an overthickened lithospheric mantle root without lower crust.

© 2014 Elsevier Ltd. All rights reserved.

1. Introduction

Granites are among the predominant rocks in the continental crust and their generation reflects the principal mechanism by which continental material is transferred from the deep crust to near the surface of the Earth. Despite the relative simplicity in their rock-forming mineral components (including mainly quartz, feldspars and minor amount of mafic minerals), the origin of their parental magma and the mechanism to form the magma is still a key subject of study (e.g., Wu et al., 2007; Wang et al., 2013a;

Tang et al., 2014). Notwithstanding strongly peraluminous (SP) granites (with A/CNK (molecular $\text{Al}_2\text{O}_3/(\text{CaO} + \text{Na}_2\text{O} + \text{K}_2\text{O})$) ratios >1.1) that indicate a direct derivation by crustal melting (e.g., Chappell and White, 1992; Patiño Douce, 1995), an increasing number of studies have revealed that some complicate processes and different source materials may have been involved in their genesis (e.g., Gray, 1984; Collins, 1996; Healy et al., 2004). It is likely that mantle-derived magma makes a crucial contribution to the generation of some SP granitoids (e.g., Belousova et al., 2006; Phillips et al., 2011), including not only the heat input but also mafic material incorporation. For example, high $\text{CaO}/\text{Na}_2\text{O}$ ratios (>0.3) along with high $(\text{FeO} + \text{MgO} + \text{TiO}_2)$ values (>4) in some SP granites can be ascribed to mixing of basaltic melts with pelite-derived melts, rather than simple anatexis of psammites (e.g., Sylvester, 1998). Also, studies on microgranitoid enclaves

* Corresponding author at: Guangzhou Institute of Geochemistry, Chinese Academy of Sciences, P.O. Box 1131, Guangzhou 510640, China. Tel.: +86 20 85290753; fax: +86 20 85291510.

E-mail address: tppeng08@126.com (T. Peng).

(e.g., Elburg, 1996; Mass et al., 1997; Waught et al., 2001) have revealed such a likely magma mixing origin for some SP granites. More importantly, isotopic signatures have evidenced that magma mixing (between crust- and mantle-derived magmas) play an important role in the genesis of some SP granites, such as the Lachlan granites in eastern (e.g., Collins, 1996; Healy et al., 2004; Belousova et al., 2006) and southeastern Australia (e.g., Gray, 1984).

The South China Block (SCB), which is one of the biggest granite provinces in the world, is characterized by exceptionally extensive occurrence of granitoid rocks with different emplacement ages and with a total exposure area up to 1,000,000 km² (e.g., Sun, 2006; Hua et al., 2013). It is well documented that numerous economically important metallic deposits (i.e., W, Sn, Nb, Ta and REE deposits) are closely associated with granites in the area (e.g., Hua et al., 2013 and references therein). Therein, the early Paleozoic granitoids that are dominated by SP granitic rocks (e.g., Wang et al., 2007, 2011; Li et al., 2010; Zhang et al., 2012b) with minor I-type granites (e.g., Huang et al., 2013; Zhao et al., 2013), are distinctly different from other granitic generations in the SCB, although the total exposure is relatively less than those of the Yanshanian granites (e.g., Sun, 2006; Hua et al., 2013). The existence of such a huge volume (up to 10,000 km²) of early Paleozoic SP granitoids in the SCB has triggered extensive discussion about its origin and genesis, particularly in recent five years (e.g., Wang et al., 2007, 2011, 2012; Li et al., 2010; Zhang et al., 2012b). Nonetheless, the genesis and tectonic implications of these granites, particularly whether the mantle-derived magmas were involved in the SP granite formation, are still unclear due to the lack of contemporaneous mafic rocks, although some authors have invoked the addition of some basic materials to account for their geochemical signatures (e.g., Wang et al., 2011; Zhang et al., 2012b).

More recently, Yao et al. (2012) and Wang et al. (2013d) have recognized some early Paleozoic mafic igneous rocks in the Wuyi–Yunkai orogen. Consequently, it is necessary to reevaluate the contribution from mantle-derived magma to the resultant formation of SP granites in the area. In particular, for the early Paleozoic SP granites that crop out along the southwestern margin of the SCB, far away from the core of the Wuyi–Yunkai orogen, whether they share a common origin and tectonic setting with those in the core of the Wuyi–Yunkai orogen needs further investigation. Furthermore, the new identification of the early Paleozoic mafic igneous rocks in the SCB provides crucial clues to better constrain the transition timing of tectonic regime from syn-orogen to post-orogen stages and likely shed light on the mechanism of post-collisional magmatism.

In this paper, we present whole-rock geochemical and Sr–Nd isotopic compositions, and zircon U–Pb dating and Lu–Hf isotope results for the early Paleozoic granites in the southeastern Yunnan, Southwestern SCB. Based on our results along with regional data, our aims are to: (1) constrain their main emplacement time; (2) provide an insight into the origin of the early Paleozoic granites, and their rock-forming regime; (3) decode the geodynamic mechanism for their generation; and (4) discuss the space–time relationships between the early Paleozoic crustal anatexis and the tectonic evolution of the Wuyi–Yunkai orogeny.

2. Geological background

The SCB consists of the Yangtze Block, in the northwest, and the Cathaysia Block, in the southeast (Fig. 1 insert), which was amalgamated during Neoproterozoic time (e.g., Li et al., 2002, 2009; Zhao and Cawood, 1999, 2012). The tectonic zone is named as the Jinning or Sibao orogen (e.g., Li et al., 2007). The present boundary between the two blocks is the northeasterly trending Jiangshan–Shaoxing Fault (Fig. 1) (e.g., Chen and Jahn, 1998; Wang et al., 2008; Zhang et al., 2012b), but the southwesterly

extension is uncertain due to poor exposure and intensive younger tectonic modification. The Yangtze basement consists predominantly of Proterozoic rocks, with minor outcrop of Archean rocks such as the Kongling complex that was dated up to ca. 3.2 Ga (e.g., Qiu et al., 2000). Neoproterozoic igneous rocks crop out widely around the Yangtze Block (e.g., Wang et al., 2006b). In the Cathaysia Block, the oldest basement rocks were the amphibolite dated at ~1.80 Ga (LA-MC-ICP-MS method) in the Wuyishan area, mainly in the northeastern portion (e.g., Li et al., 2011), although some older detrital zircons (>2.0 Ga) have also been revealed (e.g., Yu et al., 2008). In addition, minor Mesoproterozoic granitic rocks that were dated at ~1.43 Ga were also recognized in the Hainan Island, to the south (Li et al., 2002). Recently, some Neoproterozoic mafic rocks with similar ages to those around the Yangtze Block were also recognized within the Cathaysia Block (Zhang et al., 2012a).

The recognition of an angular unconformity between post-Silurian cover and strongly deformed pre-Devonian strata in the SCB indicates the occurrence of an orogenic event during early Paleozoic time. Ting (1929) initially defined the event as the Kwangssian movement, whereas other workers subsequently named it as the “Caledonian Orogeny” (e.g., Huang, 1978; Ren, 1991) or the Wuyi–Yunkai orogeny (e.g., Li et al., 2010; Zhang et al., 2012b). As for the nature of the orogeny, some researchers believed that the mountain-building event was the result of the final closure of the Huayan/Paleotethys Ocean and subsequent collision of the Yangtze and Cathaysia Blocks (e.g., Guo et al., 1989; Hsü, 1994; Chen et al., 2006; Yan et al., 2006). However, the absence of the subduction-related rock associations (e.g., ophiolites, magmatic arc, subduction complexes and high-pressure metamorphic rocks) in the whole SCB convincingly precludes the existence of an ocean basin between the Yangtze and Cathaysia Blocks during early Paleozoic time, which led some researchers to propose an intracontinental orogenic event (e.g., Charvet et al., 1996, 2010; Faure et al., 2009; Li et al., 2010). More recently, on the basis of the fact that the 460–400 Ma event was mainly restricted to the Cathaysia Block, Zhao and Cawood (2012) further suggested that the early Paleozoic (460–430 Ma) orogeny in the Cathaysia Block was a continent–continent collisional event. This resulted in the region occupied by the present-day southeastern margin (Cathaysia) of South China to have amalgamated with an unknown continental block, which later was rifted away along the Zhenghe–Dapu Fault (e.g., Gao, 1991). They thus proposed that the Cathaysia Block represented a continent–continent collisional belt during early Paleozoic time (460–430 Ma), similar to the Appalachian–Caledonian belt in North America and Europe (e.g., Dewey, 1969).

The early Paleozoic granites making up over 30% of exposures and ranging from Ordovician to Late Devonian in age (ca. 400–462 Ma; Li et al., 2010; Wang et al., 2007, 2011; Chu et al., 2012a; Zhang et al., 2012b and references therein), are mainly exposed in the Wugong, Wuyi, Baiyun and Yunkai areas. Most of them are located in the core of the Wuyi–Yunkai orogen, with minor outcrops far away from the orogen (more than 500 km; Fig. 1), such as the Xuefeng and Dulong–Song Chay granitic batholiths (e.g., Roger et al., 2000; Wang et al., 2007, 2011; Li et al., 2010; Chu et al., 2012a). Overall, all the exposed early Paleozoic granitoids show a planar-shaped distribution pattern to the east of the Anhua–Luocheng Fault, the eastern SCB (e.g., Chu et al., 2012a; Zhang et al., 2012b). Most recently, minor early Paleozoic mafic igneous rocks, including high-Mg basalts (Yao et al., 2012) and diabases and gabbros (Wang et al., 2013d) have also been recognized in the Wuyi–Yunkai orogen (Fig. 1b). These igneous rocks have been interpreted as the products of the Wuyi–Yunkai orogeny or Kwangssian orogeny (e.g., Li et al., 2010; Wang et al., 2007, 2011, 2013c; Zhang et al., 2012b; Huang et al., 2013; Zhao et al., 2013). More detailed information on the geological characteristics and field relationship in the SCB has been summarized by Li et al.

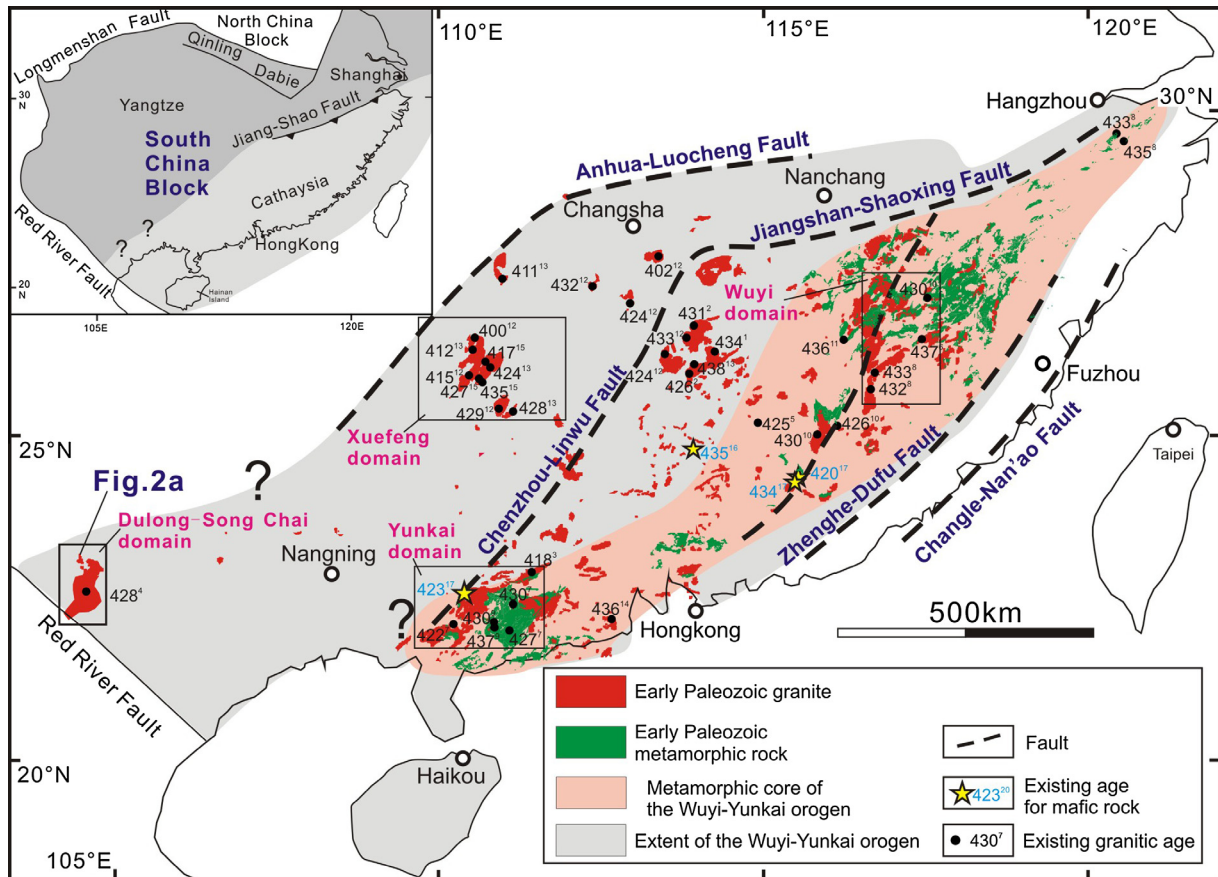


Fig. 1. Simplified geological map showing the tectonic framework of the South China Block (SCB) (modified from Li et al. (2010) and Yao et al. (2012)). Sources for granitic (shown in black dots and numbers) ages as shown in the figure are: 1 – Li et al. (1989); 2 – Li (1991); 3 – Wang et al. (1998); 4 – Roger et al. (2000); 5 – Xu et al. (2005); 6 – Liu et al. (2008); 7 – Wang et al. (2007); 8 – Li et al. (2010); 9 – Wan et al. (2010); 10 – Wang et al. (2011); 11 – Zhang et al. (2011); 12 – Zhang et al. (2012b); 13 – Chu et al. (2012); 14 – Huang et al. (2013); 15 – Zhao et al. (2013); 16 – Yao et al. (2012); 17 – Wang et al. (2013d). The insert shows the relationship between the Yangtze and Cathaysia Blocks.

(2010) and other workers (e.g., Wang et al., 2011, 2012, 2013d; Zhao et al., 2013).

The Dulong–Song Chay batholith lies in the southwestern Cathaysia Block (Fig. 1). The Indochina Block and the Ailaoshan–Red River Fault are west of it. The batholith is a metamorphic complex composed mainly of migmatites, porphyroid granites and augen gneisses resulting from the deformation of these granites (Roger et al., 2000; Yan et al., 2006). The metamorphism and deformation took place during the Indosinian and Cenozoic events (YNBGM, 1976; Yan et al., 2006; Guo et al., 2009). These deformed granitic rocks are gray to light gray and medium to fine grained with blasto-quasiporphyritic textures and augen and gneissic structures. They have similar mineral assemblages, including main minerals of quartz, plagioclase, K-feldspar and mica and minor accessory minerals of zircon, apatite and sulfide minerals. All facies are biotite-bearing, and in some places also muscovite-bearing. K-feldspar augen are generally ~1 cm long (partly up to 6 cm long; Fig. 3a and b). In some places the augen granite was strongly mylonitized (Fig. 3c), and minor granites give a massive appearance of a relatively uniform, medium-grained, magmatic rock (Fig. 3d).

The Dulong–Song Chay batholith is the largest one in the southwestern part of the SCB. It straddles the Vietnam–Yunnan border and its total outcrop area is up to ca. 7000 km² (Fig. 2a). The Dulong and Song Chay batholiths were referred to as the segments in China (e.g., Yan et al., 2006) and in Vietnam (e.g., Roger et al., 2000), respectively (Fig. 2a). Roger et al. (2000) obtained an upper

intercept age of 428 ± 5 Ma based on seven zircon grains from the granite in the Song Chay area, representing the age of granite emplacement. The dated sample is a deformed orthogneiss containing large microcline porphyroclasts (~1 cm), biotites and white micas. Yan et al. (2006) reported two granitic gneisses within the Dulong core complex with the ages of 436–402 Ma, which were generally transformed into moderately deformed gneisses bearing large (1–10 cm) feldspar augens. To date, no chemical or isotopic data for these granitic rocks have been reported. The Dulong–Song Chay batholith experienced multiple tectonothermal modifications. The geological features and evolution, including the components and metamorphic and deformational histories in the whole complex, have been described in detail by Roger et al. (2000), Yan et al. (2006) and Hung (2010).

In this study, we conducted a systematic investigation on the Dulong batholith in southeastern Yunnan, southwestern Cathaysia Block. The granitic batholith was emplaced into the Lower Paleozoic metasedimentary rocks with a low-grade metamorphism (Fig. 2b) (e.g., Roger et al., 2000; Yan et al., 2006). These units are dominated by limestone and dolomitic limestone, more than 9000 m thick, with minor interbedded siltstone, phyllite and slate, which is of Cambrian age in its upper part (e.g., YNBGM, 1976; Roger et al., 2000; Yan et al., 2006). The Ordovician sedimentary rocks consist of limestone in the lower segment, with a thickness of ~450 m and >1200 m-thick siltstone in the middle-upper segment (YNBGM, 1976).

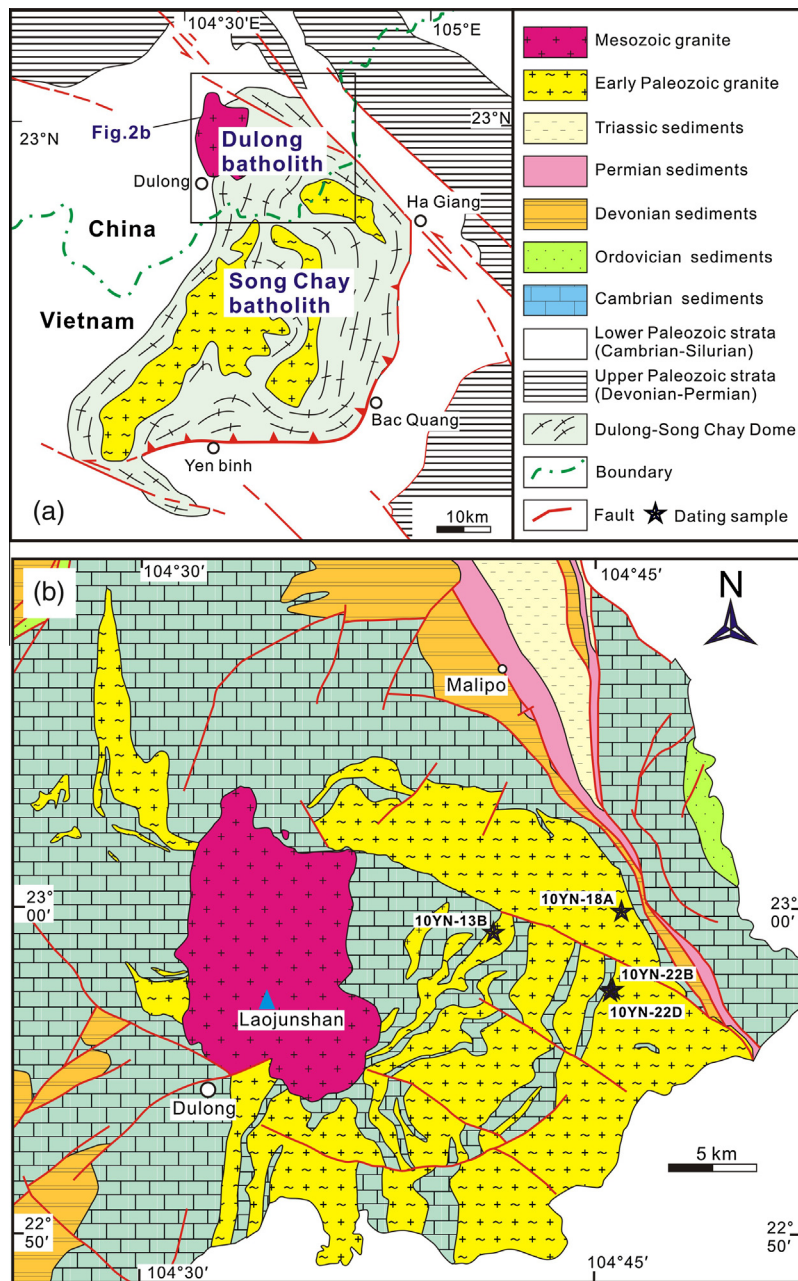


Fig. 2. Simplified geological maps of (a) the Dulong-Song Chay batholith (modified after Roger et al., 2000) and (b) the Dulong Batholith (modified after Maguan Geological Map at 1:200,000 scale; YNBGMR, 1976), showing rock types and dating sample locations.

3. Sampling and petrography

In this study, four gneissic granite samples were collected for LA-ICP-MS zircon U-Pb dating from the Dulong batholith, Southwestern SCB (Fig. 2b). They were sampled from the Malipo-Nanwenhe (10YN-13B: N22°59.623', E104°41.651') and Jiaozicheng-Bazi (10YN-18A: N22°59.923', E104°46.381') old roads, and jiaozicheng-Mengdong (10YN-22B: N22°57.218', E104°45.997') and Lancang-Simao (10YN-22D: N22°57.218', E104°45.997') highways (Fig. 2b). Three samples of them were generally transformed into moderately deformed gneisses bearing large (1–10 cm) feldspar augens (Fig. 3a–c), while the sample 10YN-22D was slightly deformed and show a missive structure (Fig. 3d).

The mineralogy of the four granites is similar and characterized by K-feldspar (~25–35 vol.%), plagioclase (~27–36 vol.%), quartz (~16–32 vol.%), biotite (~4–8 vol.%), muscovite (~4–8 vol.%) and

minor amount of zircon, apatite, titanite and iron oxides. Therein, most of fine-grained muscovites in some samples are secondary, whereas the coarse-grained ones clearly indicate a magmatic origin. Based on modal mineral compositions obtained by point counting and then plotting on a QAP diagram (Fig. 4), most of the studied samples plot in the monzogranite field, excepting one sample that straddles the boundary between the monzogranite and granodiorite fields.

4. Analytical techniques

4.1. Zircon U-Pb isotope analysis

Zircons for LA-ICP-MS U-Pb dating were separated from all samples by using conventional heavy liquid and magnetic tech-

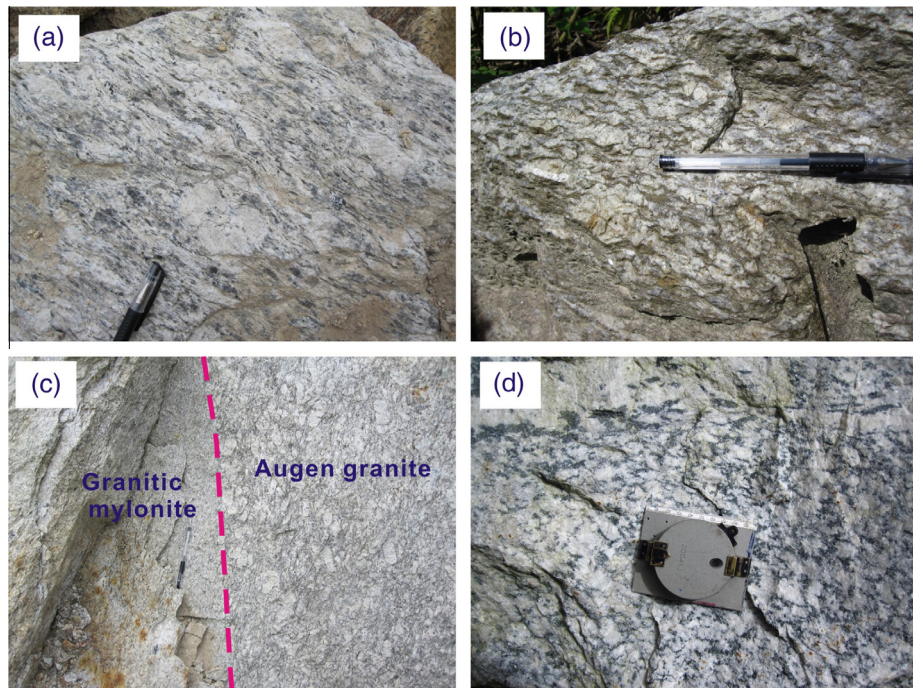


Fig. 3. Photographs of the representative granitic rocks from the Dulong area: (a) sample 10YN-13B, augen granite: K-feldspar phenocrysts (up to 6 cm long and 3 cm wide) are wrapped by bands of quartz, muscovite, and biotite forming augen structures. (b) Sample 10YN-18A augen granite, similar to the sample 10YN-13B. (c) Sample 10YN-22B, augen granite which is contacted with granitic mylonite. (d) Sample 10YN-22D, a relatively unstrained gneissic granite.

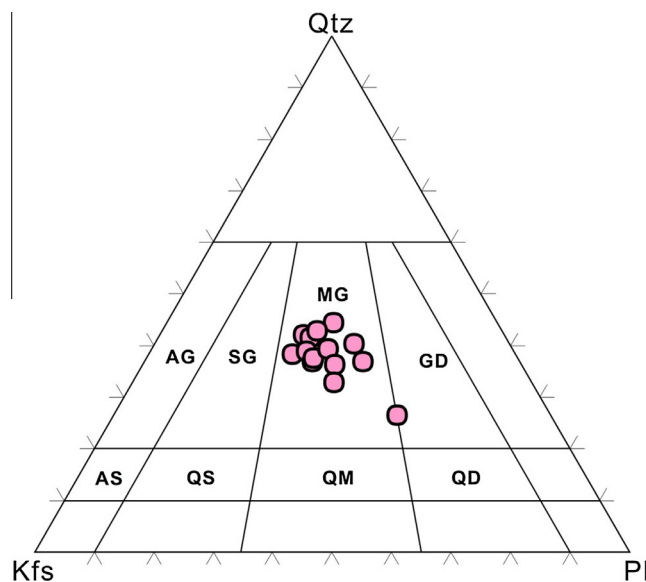


Fig. 4. Modal classification of the granitoids (after Streckeisen, 1967). AG = alkali-feldspar granite; AS = alkali-feldspar syenite; SG = syenogranite; QS = quartz syenite; MG = monzogranite; QM = quartz monzonite; GD = granodiorite; QD = quartz monzonodiorite.

niques and purified by handpicking under a binocular microscope. The zircon grains were mounted in epoxy resin, polished to half their thickness, and gold coated, and then photographed in transmitted and reflected light. The internal structure of zircons was examined using cathodoluminescence (CL) imaging prior to U-Pb isotopic analysis. The CL images were obtained using an EMPA-JXA-8100 scanning electron microscope at the Guangzhou Institute of Geochemistry, Chinese Academy of Sciences, Guangzhou. U-Pb dating of zircon was conducted by LA-ICP-MS at the State Key Laboratory of Ore Deposit Geochemistry, Institute of Geochemistry,

Chinese Academy of Sciences, Guiyang, China. A GeoLasPro laser-ablation system (Lambda Physik, Gottingen, Germany) and Agilent 7700x ICP-MS (Agilent Technologies, Tokyo, Japan) were combined for the experiments. The 193 nm ArF excimer laser, homogenized by a set of beam delivery systems, was focused on the zircon surface with fluence of 10 J/cm^2 . Ablation protocol employed a spot diameter of $32 \mu\text{m}$ at 5 Hz repetition rate for 40 s (equating to 200 pulses). Helium was the carrier gas used to transport aerosols to the ICP-MS. Zircon 91500 ($^{206}\text{Pb}/^{238}\text{U}$ age = $1062.4 \pm 0.8 \text{ Ma}$; Wiedenbeck et al., 1995) was used as the external standard to correct for elemental fractionation, while zircons GJ-1 ($^{207}\text{Pb}/^{206}\text{Pb}$ age = $608.5 \pm 0.4 \text{ Ma}$; Jackson et al., 2004) and Plešovice ($^{206}\text{Pb}/^{238}\text{U}$ age = $337.3 \pm 0.4 \text{ Ma}$; Slama et al., 2008) were also used for quality control. Lead concentration in zircon was externally calibrated against NIST SRM 610 with Si as the internal standard, and Zr as the internal standard for other trace elements (Hu et al., 2011). Data reduction was performed off-line by ICPMSDataCal (Liu et al., 2010a,b). ^{202}Hg is usually $<10 \text{ cps}$ in the gas blank, therefore the contribution of ^{204}Hg to ^{204}Pb is negligible and is not considered further. Common Pb was corrected according to the method proposed by Anderson (2002). The U-Pb ages were calculated using the U decay constants of Steiger and Jäger (1997) and Isoplot Ex 3 software (Ludwig, 2003). Individual analyses are presented with 1σ error (95% confidence level) in Table 1. U-Pb zircon results are listed in Table 1, and the representative zircon CL images and their U-Pb concordia plots are shown in Figs. 5 and 6.

4.2. Zircon Hf isotope analysis

All Hf isotopic compositions of single-grain zircons were determined at the Department of Earth Sciences, the University of Hong Kong. The detailed analytical procedure follows that reported by Xia et al. (2011). Standard zircon 91500 was used as the reference standard, with a weighted mean $^{176}\text{Hf}/^{177}\text{Hf}$ ratio of 0.282314 ± 0.000018 ($n = 50$, 2σ) in this study. Correction for isobaric interference of ^{176}Lu on ^{176}Hf and ^{176}Yb on ^{176}Hf was

Table 1

LA-ICP-MS U-Pb data for zircons from the Dulong granites in the western SCB.

Analysis	Content (ppm)			Th/U	Corrected isotope ratios					Isotope ages (Ma)						
	Th	U	Pb ^a		$^{207}\text{Pb}^{\text{a}}/^{206}\text{Pb}^{\text{a}}$	$\pm 1\sigma$	$^{207}\text{Pb}^{\text{a}}/^{235}\text{U}$	$\pm 1\sigma$	$^{206}\text{Pb}^{\text{a}}/^{238}\text{U}$	$\pm 1\sigma$	$^{207}\text{Pb}^{\text{a}}/^{206}\text{Pb}^{\text{a}}$	$\pm 2\sigma$	$^{207}\text{Pb}^{\text{a}}/^{235}\text{U}$	$\pm 2\sigma$	$^{206}\text{Pb}^{\text{a}}/^{238}\text{U}$	$\pm 2\sigma$
<i>10YN-13B</i>																
YN13B-01	136	1040	63.5	0.13	0.0552	0.0012	0.5250	0.0093	0.0687	0.0008	420	53	428	6	429	5
YN13B-02	58.7	321	20.8	0.18	0.0554	0.0019	0.5268	0.0172	0.0688	0.0012	432	78	430	11	429	7
YN13B-03	76.9	341	22.6	0.23	0.0551	0.0014	0.5260	0.0127	0.0689	0.0006	417	53	429	8	429	4
YN13B-04	122	1302	78.7	0.09	0.0551	0.0007	0.5272	0.0073	0.0688	0.0006	413	28	430	5	429	4
YN13B-05	134	476	33.2	0.28	0.0555	0.0018	0.5450	0.0161	0.0709	0.0008	432	68	442	11	442	5
YN13B-06	749	675	75.6	1.11	0.0548	0.0014	0.5252	0.0136	0.0687	0.0006	406	57	429	9	428	4
YN13B-07	58.7	413	25.9	0.14	0.0554	0.0019	0.5418	0.0170	0.0705	0.0008	428	76	440	11	439	5
YN13B-08	98.7	1535	90.2	0.06	0.0545	0.0014	0.5309	0.0135	0.0694	0.0007	391	56	432	9	432	4
YN13B-09	70.6	289	31.4	0.24	0.0603	0.0019	0.9023	0.0284	0.1065	0.0015	613	69	653	15	652	9
YN13B-10	158	1280	78.8	0.12	0.0540	0.0025	0.5253	0.0183	0.0692	0.0017	372	106	429	12	431	10
YN13B-11	112	962	59.3	0.12	0.0543	0.0033	0.5260	0.0281	0.0688	0.0009	383	140	429	19	429	5
YN13B-12	159	956	60.6	0.17	0.0541	0.0031	0.5258	0.0257	0.0689	0.0007	376	131	429	17	429	4
YN13B-13	234	820	61.1	0.29	0.0546	0.0037	0.5490	0.0305	0.0713	0.0013	398	150	444	20	444	8
YN13B-14	93.9	1366	81.5	0.07	0.0543	0.0066	0.5308	0.0622	0.0690	0.0007	383	278	432	41	430	4
YN13B-15	106	498	33.2	0.21	0.0553	0.0054	0.5341	0.0407	0.0693	0.0018	433	218	435	27	432	11
YN13B-16	140	379	29.7	0.37	0.0550	0.0044	0.5649	0.0409	0.0730	0.0018	409	184	455	27	454	11
YN13B-17	133	223	18.4	0.60	0.0549	0.0042	0.5274	0.0415	0.0684	0.0021	409	172	430	28	426	13
YN13B-18	104.6	419	29.3	0.25	0.0550	0.0034	0.5257	0.0303	0.0687	0.0015	413	105	429	20	429	9
YN13B-19	102.7	281	20.6	0.37	0.0552	0.0026	0.5267	0.0235	0.0687	0.0011	420	106	430	16	428	7
YN13B-20	54.9	302	19.5	0.18	0.0547	0.0015	0.5244	0.0148	0.0686	0.0006	467	58	428	10	428	4
<i>10YN-18A</i>																
YN18A-01	137	570	38.0	0.24	0.0551	0.0015	0.5262	0.0137	0.0689	0.0007	417	61	429	9	429	4
YN18A-02	91.6	971	58.0	0.09	0.0551	0.0010	0.5269	0.0097	0.0689	0.0006	417	41	430	6	429	3
YN18A-03	234	1052	68.7	0.22	0.0550	0.0009	0.5267	0.0088	0.0689	0.0005	413	37	430	6	429	3
YN18A-04	109	664	41.8	0.16	0.0551	0.0009	0.5267	0.0089	0.0689	0.0004	417	39	430	6	430	3
YN18A-05	76.6	793	46.9	0.10	0.0556	0.0017	0.5310	0.0156	0.0688	0.0009	435	69	432	10	429	5
YN18A-06	109	1433	83.1	0.08	0.0552	0.0019	0.5234	0.0139	0.0686	0.0017	420	78	427	9	428	11
YN18A-07	121	528	36.4	0.23	0.0556	0.0012	0.5520	0.0115	0.0717	0.0005	435	48	446	8	446	3
YN18A-08	48.0	578	34.0	0.08	0.0551	0.0022	0.5260	0.0203	0.0688	0.0010	417	91	429	13	429	6
YN18A-09	49.5	439	27.0	0.11	0.0557	0.0016	0.5487	0.0159	0.0713	0.0012	439	65	444	10	444	7
YN18A-10	158	308	26.2	0.51	0.0564	0.0016	0.5844	0.0152	0.0752	0.0007	478	32	467	10	467	4
YN18A-11	110	1505	87.1	0.07	0.0554	0.0024	0.5264	0.0188	0.0685	0.0011	432	96	429	12	427	7
YN18A-12	112	451	34.5	0.25	0.0562	0.0016	0.6034	0.0170	0.0773	0.0007	461	61	479	11	480	4
YN18A-13	61.5	388	23.8	0.16	0.0552	0.0009	0.5268	0.0087	0.0689	0.0006	420	37	430	6	430	3
YN18A-14	109	735	44.4	0.15	0.0550	0.0009	0.5265	0.0083	0.0689	0.0005	413	40	430	5	429	3
YN18A-15	95.0	811	51.0	0.12	0.0557	0.0012	0.5666	0.0113	0.0733	0.0007	439	46	456	7	456	4
YN18A-16	116	745	43.8	0.16	0.0560	0.0028	0.5341	0.0197	0.0690	0.0030	454	111	435	13	430	18
YN18A-17	75.8	781	45.4	0.10	0.0550	0.0011	0.5269	0.0098	0.0690	0.0006	413	43	430	7	430	3
YN18A-18	104	726	43.7	0.14	0.0549	0.0011	0.5276	0.0108	0.0690	0.0006	409	46	430	7	430	3
YN18A-19	269	498	40.8	0.54	0.0547	0.0013	0.5260	0.0120	0.0689	0.0005	467	52	429	8	430	3
YN18A-20	79.5	761	44.4	0.10	0.0549	0.0008	0.5268	0.0075	0.0689	0.0004	409	33	430	5	430	3
YN18A-21	317	824	60.4	0.38	0.0549	0.0008	0.5265	0.0075	0.0689	0.0004	406	33	429	5	430	3
YN18A-22	299	1026	73.1	0.29	0.0553	0.0009	0.5569	0.0090	0.0722	0.0004	433	39	450	6	449	3
<i>10YN-22B</i>																
YN22B-01	207.0	120	3749	0.03	0.0546	0.0011	0.5269	0.0127	0.0690	0.0009	394	48	430	8	430	5
YN22B-02	100.9	195	1691	0.12	0.0547	0.0010	0.5257	0.0092	0.0688	0.0005	467	38	429	6	429	3
YN22B-03	26.62	84.6	422	0.20	0.0550	0.0013	0.5233	0.0118	0.0686	0.0006	413	56	427	8	427	4
YN22B-04	68.18	89.9	1192	0.08	0.0548	0.0010	0.5263	0.0096	0.0688	0.0006	406	47	429	6	429	3

YN22B-05	47.43	55.6	824	0.07	0.0548	0.0012	0.5278	0.0113	0.0691	0.0006	406	52	430	8	431	4
YN22B-06	32.43	65.9	466	0.14	0.0565	0.0013	0.6201	0.0142	0.0789	0.0007	472	54	490	9	490	4
YN22B-07	30.02	102.9	462	0.22	0.0548	0.0021	0.5255	0.0200	0.0687	0.0008	406	83	429	13	428	5
YN22B-08	84.2	135	1457	0.09	0.0550	0.0020	0.5248	0.0167	0.0687	0.0013	413	83	428	11	428	8
YN22B-09	19.19	64.8	303	0.21	0.0550	0.0022	0.5243	0.0197	0.0687	0.0008	413	89	428	13	428	5
YN22B-10	35.07	59.3	584	0.10	0.0550	0.0034	0.5238	0.0294	0.0686	0.0010	413	106	428	20	428	6
YN22B-11	33.01	77.1	533	0.14	0.0551	0.0009	0.5275	0.0087	0.0689	0.0005	417	39	430	6	430	3
YN22B-12	97.80	68.9	1645	0.04	0.0554	0.0015	0.5626	0.0149	0.0729	0.0009	428	61	453	10	453	5
YN22B-13	32.96	88.7	526	0.17	0.0553	0.0009	0.5299	0.0087	0.0688	0.0005	433	35	432	6	429	3
YN22B-14	156.4	157	2760	0.06	0.0548	0.0011	0.5250	0.0097	0.0687	0.0007	406	44	429	6	428	4
YN22B-15	50.08	104	836	0.12	0.0556	0.0009	0.5322	0.0084	0.0689	0.0007	435	3	433	6	429	4
YN22B-16	25.55	88.6	391	0.23	0.0552	0.0013	0.5268	0.0120	0.0689	0.0007	420	54	430	8	429	4
YN22B-17	38.7	505	261	1.94	0.0553	0.0015	0.5233	0.0137	0.0686	0.0007	433	58	427	9	427	4
YN22B-18	87.7	517	1218	0.42	0.0549	0.0008	0.5228	0.0076	0.0685	0.0005	409	33	427	5	427	3
YN22B-19	115.9	115	2050	0.06	0.0549	0.0007	0.5266	0.0068	0.0689	0.0004	409	25	430	5	429	2
YN22B-20	43.14	55.2	747	0.07	0.0550	0.0016	0.5241	0.0142	0.0686	0.0006	413	63	428	9	428	4
YN22B-21	18.56	43.0	303	0.14	0.0549	0.0011	0.5275	0.0114	0.0690	0.0006	409	44	430	8	430	3
YN22B-22	88.3	105	1529	0.07	0.0551	0.0014	0.5275	0.0121	0.0688	0.0009	417	55	430	8	429	5
YN22B-23	81.5	596	969	0.62	0.0550	0.0021	0.5294	0.0202	0.0691	0.0009	413	83	431	13	431	5
YN22B-24	23.7	130	288	0.45	0.0558	0.0024	0.5678	0.0247	0.0734	0.0010	443	127	457	16	457	6
YN22B-25	129.5	165	2127	0.08	0.0554	0.0018	0.5559	0.0186	0.0721	0.0008	428	72	449	12	449	5
YN22B-26	36.77	78.4	575	0.14	0.0559	0.0017	0.5681	0.0174	0.0732	0.0013	450	69	457	11	455	8
YN22B-27	59.77	81.1	1005	0.08	0.0550	0.0024	0.5230	0.0243	0.0686	0.0014	413	92	427	16	428	8
YN22B-28	27.6	95	411	0.23	0.0554	0.0021	0.5393	0.0209	0.0703	0.0009	428	85	438	14	438	6
YN22B-29	28.96	62.1	459	0.14	0.0555	0.0018	0.5274	0.0170	0.0690	0.0009	432	69	430	11	430	5
YN22B-30	91.40	74.9	1525	0.05	0.0558	0.0021	0.5627	0.0233	0.0727	0.0007	443	81	453	15	452	4
<i>10YN-22D</i>																
YN22D-01	54.56	73.5	932	0.08	0.0551	0.0019	0.5257	0.0193	0.0688	0.0007	417	75	429	13	429	4
YN22D-02	57.04	83.5	979	0.09	0.0552	0.0013	0.5267	0.0127	0.0688	0.0005	420	52	430	8	429	3
YN22D-03	69.5	106	1150	0.09	0.0553	0.0014	0.5457	0.0134	0.0710	0.0005	433	56	442	9	442	3
YN22D-04	142.8	165	2513	0.07	0.0548	0.0013	0.5207	0.0140	0.0682	0.0015	406	52	426	9	425	9
YN22D-05	58.5	121	923	0.13	0.0557	0.0012	0.5694	0.0116	0.0736	0.0007	439	48	458	8	458	4
YN22D-06	34.9	108	561	0.19	0.0551	0.0009	0.5240	0.0090	0.0685	0.0005	417	32	428	6	427	3
YN22D-07	36.0	153	504	0.30	0.0554	0.0018	0.5535	0.0188	0.0718	0.0008	428	74	447	12	447	5
YN22D-08	66.8	378	919	0.41	0.0550	0.0013	0.5271	0.0121	0.0689	0.0006	413	52	430	8	430	4
YN22D-09	78.5	1143	444	2.58	0.0561	0.0031	0.5201	0.0260	0.0682	0.0023	457	122	425	17	425	14
YN22D-10	76.4	150	1288	0.12	0.0552	0.0017	0.5269	0.0153	0.0689	0.0007	420	69	430	10	430	4
YN22D-11	76.4	342	1016	0.34	0.0562	0.0018	0.5774	0.0178	0.0743	0.0009	461	70	463	11	462	5
YN22D-12	54.8	106	838	0.13	0.0558	0.0016	0.5707	0.0175	0.0737	0.0006	456	58	458	11	458	4
YN22D-13	53.3	150	887	0.17	0.0552	0.0029	0.5225	0.0236	0.0685	0.0030	420	117	427	16	427	18
YN22D-14	386.1	237	6977	0.03	0.0553	0.0028	0.5325	0.0258	0.0694	0.0004	433	111	433	17	432	3
YN22D-15	135.8	138	2284	0.06	0.0554	0.0015	0.5595	0.0162	0.0726	0.0006	432	66	451	11	452	4
YN22D-16	181.4	174	3036	0.06	0.0553	0.0019	0.5526	0.0183	0.0718	0.0011	433	76	447	12	447	7
YN22D-17	72.4	188	1179	0.16	0.0555	0.0024	0.5330	0.0251	0.0689	0.0018	432	98	434	17	430	11
YN22D-18	173.2	489	2695	0.18	0.0548	0.0020	0.5265	0.0148	0.0688	0.0013	406	80	429	10	429	8
YN22D-19	109.1	126	1912	0.07	0.0547	0.0013	0.5282	0.0131	0.0690	0.0009	398	56	431	9	430	6
YN22D-20	41.4	143	647	0.22	0.0546	0.0016	0.5231	0.0143	0.0685	0.0010	394	65	427	10	427	6

^a Radiogenic lead.

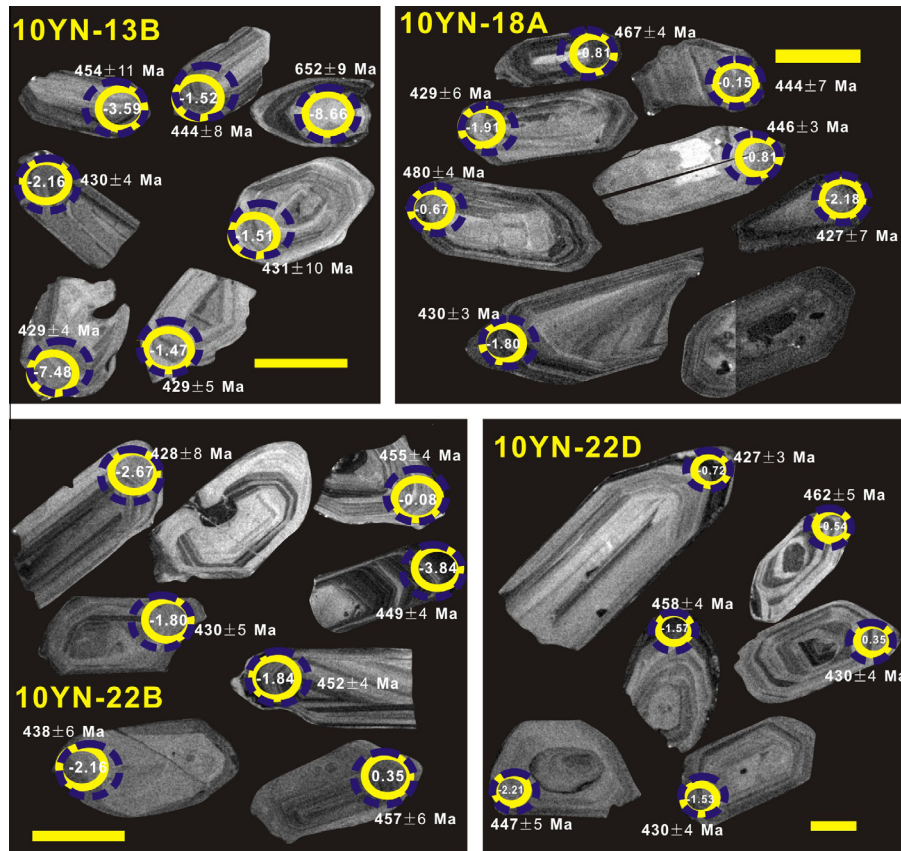


Fig. 5. Cathodoluminescence images of representative zircons from the Dulong granitic rocks. Scale bar = 100 μm ; small circles are of laser U-Pb analysis and large circles of Hf isotope analysis; the numbers in the inner and outer circles represent the $\epsilon_{\text{Hf}}(t)$ values and U-Pb ages, respectively.

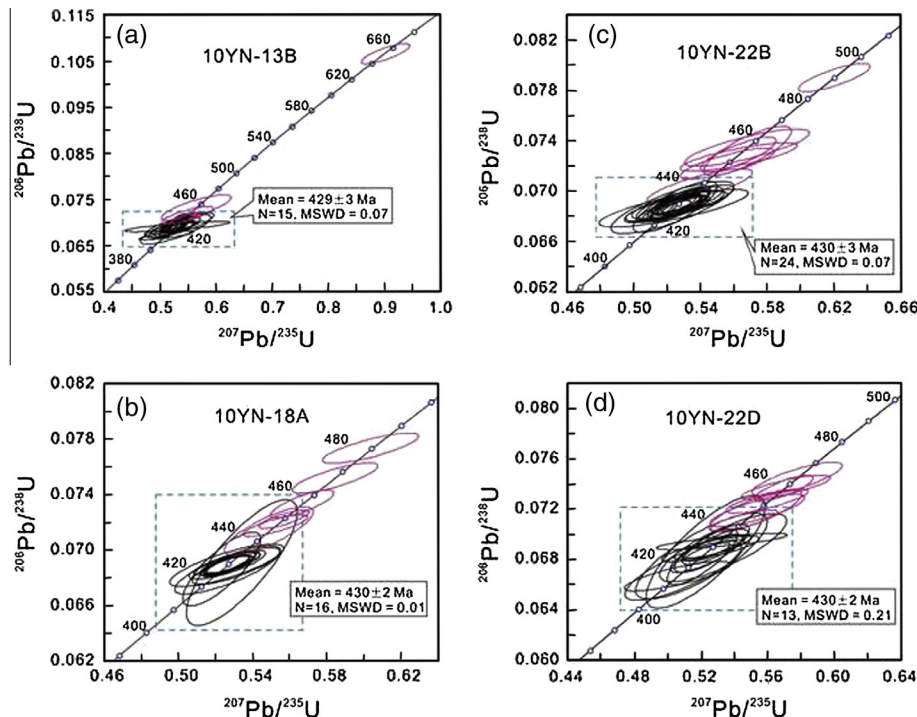


Fig. 6. LA-ICP-MS zircon U-Pb concordia plots for the early Paleozoic granites from the Dulong batholith ((a)–(d)) are the samples 10YN-13B, 10YN-18A, 10YN-22B and 10YN-22D, respectively). The black circles represent the data that were used to calculate the youngest age for every sample, while the red circles are the data of inherited or xenolith zircons.

performed by using the recommended $^{176}\text{Lu}/^{175}\text{Lu}$ ratio of 0.02669 (De and Taylor, 1993) and $^{176}\text{Yb}/^{172}\text{Yb}$ ratio of 0.5886 (Chu et al., 2002), respectively. A decay constant for ^{176}Lu of 1.865×10^{-11} year $^{-1}$ (Scherer et al., 2001) was adopted in this work. $\varepsilon_{\text{Hf}}(t)$ values were calculated using the measured U-Pb ages and with reference to the chondritic reservoir (CHUR) present-day $^{176}\text{Hf}/^{177}\text{Hf} = 0.282772$ and $^{176}\text{Lu}/^{177}\text{Hf} = 0.0332$ (Blichert-Toft and Albarede, 1997). Single-stage Hf model ages ($T_{\text{DM1}}(\text{Hf})$) were calculated relative to the depleted mantle present-day value of $^{176}\text{Hf}/^{177}\text{Hf} = 0.28325$ and $^{176}\text{Lu}/^{177}\text{Hf} = 0.0384$ (Vervoort and Blichert-Toft, 1999; Griffin et al., 2000). We also calculated a ‘crustal’ model age ($T_{\text{DM2}}(\text{Hf})$), which assumes that the parental magma was produced from average continental crust ($^{176}\text{Lu}/^{177}\text{Hf} = 0.015$) that originally was derived from the depleted mantle. The zircon Hf analyses were obtained using the same mounts as those used for U-Pb dating and data were collected over the U-Pb spots in most cases but, where this was not possible, they were run on adjacent sites within the same CL domain. The analytical results are listed in Table 2.

4.3. Major and trace element analyses

Major oxide contents were determined at the Guangzhou Institute of Geochemistry, Chinese Academy of Sciences (CAS), Guangzhou, using a wavelength X-ray fluorescence (XRF) spectrometer with analytical errors better than 2%. Trace element analyses were performed at the Institute of Geochemistry, CAS, Guiyang, China, by inductively-coupled plasma mass spectrometry (ICP-MS). The detailed analytical protocol is described in Qi et al. (2000). The analytical precision is better than 5% for elements >10 ppm, better than 8% for those <10 ppm, and about 10% for transition metals. The analytical results are presented in Table 3.

4.4. Whole-rock Sr-Nd isotope analyses

Sr and Nd isotopic compositions were measured using a Triton Thermal Ionization Mass Spectrometry (TIMS) and a Micromass Isoprobe multi-collector-inductively coupled plasma-mass spectrometer (MC-ICP-MS) at GIGCAS, respectively. Analytical procedures for Sr and Nd isotopes are described in detail by Li et al. (2004) and Chen et al. (2010). The $^{87}\text{Sr}/^{86}\text{Sr}$ value of the NBS987 standard and the $^{143}\text{Nd}/^{144}\text{Nd}$ value of the JNDI-1 standard were 0.710288 ± 28 (2σ) and 0.512109 ± 12 (2σ), respectively; fractionation corrections of $^{146}\text{Nd}/^{144}\text{Nd} = 0.7219$ and $^{86}\text{Sr}/^{88}\text{Sr} = 0.1194$ were applied to all measured $^{143}\text{Nd}/^{144}\text{Nd}$ and $^{86}\text{Sr}/^{88}\text{Sr}$ values, respectively. The Sr-Nd isotopic analytical results are presented in Table 4.

5. Results

5.1. Zircon U-Pb ages and Lu-Hf results

Zircons that were separated from four gneissic granites from the Dulong batholith are generally similar in form. They comprise predominantly subhedral to euhedral grains or grain fragments with up to 100–400 μm in length and with length/width ratios of 1:1–4:1 (Fig. 5). Most crystals are light brown or brown, prismatic and transparent to subtransparent, and show fine oscillatory growth zonation in CL images, indicative of magmatic origin (Fig. 5). Minor grains display core-mantle structure with a CL-dark or CL-bright core (unzoned) than the mantle in CL images (Fig. 5).

Ninety-two analyses on 92 grains from four samples show an age range from 426 to 652 Ma, with Th/U ratios varying from 0.03 to 2.58 (Table 1). All analyses are concordant and the young magmatic zircons define the crystallization age of the granites,

including the weighted mean $^{206}\text{Pb}/^{238}\text{U}$ ages of 429 ± 3 Ma (10YN-13B), 430 ± 2 Ma (10YN-18A), 430 ± 3 Ma (10YN-22B) and 430 ± 2 Ma (10YN-22D) (Table 1 and Fig. 6a–d). The oldest age of 652 ± 9 Ma was obtained from the zircon core (Fig. 5), indicating inheritance. Other old ages ranging from 445 to 490 Ma were obtained from the rim of magmatic zircon, likely indicating accidental xenolith that did not have time to dissolve during magma ascent (Villaros et al., 2009) (Fig. 5 and Table 1).

All ninety-two zircon grains from the four samples were analyzed for Lu-Hf isotopic composition (Table 2). All analyses yielded a relatively low $^{176}\text{Hf}/^{177}\text{Hf}$ ratios between 0.282134 and 0.282550 and a wide range of $\varepsilon_{\text{Hf}}(t)$ values from -10.09 to $+2.31$ (Table 2; Fig. 7), with $T_{\text{DM2}}(\text{Hf})$ model ages ranging from 1.35 Ga to 2.13 Ga. Most analyses with a $^{206}\text{Pb}/^{238}\text{U}$ age of ~ 430 Ma have slightly variable $\varepsilon_{\text{Hf}}(t)$ values of -5 to $+2$, with the exception of one sample up to $+2.31$ and two below -5 (Table 2).

5.2. Major and trace element data

The Dulong granitic rocks have variable major element contents (Table 3). Most of them have high $\text{K}_2\text{O}/\text{Na}_2\text{O}$ ratios (1.23–2.26) with the exception of two samples ($\text{K}_2\text{O}/\text{Na}_2\text{O} < 1.0$), showing that most of them belong to the high-K calc-alkaline series with one plotted within the shoshonite field (Fig. 8a). They have a wide range of A/CNK values (mol. $\text{Al}_2\text{O}_3/(\text{CaO} + \text{K}_2\text{O} + \text{Na}_2\text{O})$) of 1.06–1.33, most of which are >1.1 , indicating strongly peraluminous affinity (Fig. 8b; Sylvester, 1998; Clemens, 2003). On the CAF plot (Fig. 8c), all granites plot within the field of S-type granite. Moreover, their low Na_2O contents (<3.2 wt.%) in most samples are similar to that of S-type granite (Chappell and White, 1974, 2001), which is consistent with the classification of Chappell and White (1992) (Fig. 8c).

On the Harker diagrams (Fig. 9a–f), the Al_2O_3 , FeOt , CaO , MgO , and TiO_2 contents for all samples exhibit a strong decrease with increasing SiO_2 contents, with the exception of a weakly positive correlation between the P_2O_5 and SiO_2 (Fig. 9e). Such an increase in P_2O_5 with increasing SiO_2 is also an important feature of S-type granites (e.g., Chappell, 1999). All granite samples have similar chondrite-normalized REE patterns, showing enrichment in LREE (i.e., $(\text{La/Yb})_{\text{CN}} = 1.28\text{--}12.3$) with strong negative Eu anomalies ($\text{Eu}^*/\text{Eu} = 0.07\text{--}0.43$) and slightly fractionated HREE patterns ($(\text{Gd/Yb})_{\text{CN}} = 1.19\text{--}2.03$) (Fig. 10a). In the primitive mantle-normalized spidergram, they show negative Ba, Nb, Sr, P, and Ti anomalies (Fig. 10b).

5.3. Whole rock Sr-Nd isotopes

The Dulong granites have high and variable $^{87}\text{Sr}/^{86}\text{Sr}$ ratios (0.752914–0.984095) and low $^{143}\text{Nd}/^{144}\text{Nd}$ ratios (0.512118–0.512346) (Table 4). The initial $^{87}\text{Sr}/^{86}\text{Sr}$ ratios vary from 0.7149 to 0.7459, and $\varepsilon_{\text{Nd}}(t = 430 \text{ Ma})$ values range from -7.32 to -6.23 , $\varepsilon_{\text{Nd}}(t)$ values of which are slightly higher than those of the early Paleozoic I-type granites in the SCB (Fig. 11a). Their T_{DM2} model ages are in the range of 1.67–1.83 Ga (Table 4), which is distinctly younger than those of the early Paleozoic (Cambrian–Ordovician) sedimentary rocks and the Proterozoic metasedimentary rocks in the Yangtze Block (Fig. 11b).

6. Discussion

6.1. Emplacement age of the Dulong–Song Chay batholith and its significance

The Dulong–Song Chay granitic batholith underwent intense deformation and low-grade metamorphism due to multiple

Table 2

Lu–Hf isotopic compositions of zircons from the Dulong granites in the western SCB.

Analysis	$^{176}\text{Hf}/^{177}\text{Hf}$	$\pm 1\sigma$	$^{176}\text{Lu}/^{177}\text{Hf}$	$^{176}\text{Yb}/^{177}\text{Hf}$	$^{206}\text{Pb}/^{238}\text{U}$	age (Ma)	$^{176}\text{Hf}/^{177}\text{Hf}$ (i)	$\varepsilon_{\text{Hf}}(t)$	$T_{\text{DM1}}(\text{Hf})$ (Ga)	$T_{\text{DM2}}(\text{Hf})$ (Ga)	$f_{\text{Lu/Hf}}$
<i>10YN-13B</i>											
YN13B-01	0.282446	0.000015	0.000290	0.016069	429		0.282444	-2.18	1.12	1.55	-0.99
YN13B-02	0.282458	0.000012	0.001420	0.062237	429		0.282447	-2.07	1.14	1.54	-0.96
YN13B-03	0.282457	0.000012	0.001578	0.069084	429		0.282445	-2.14	1.14	1.55	-0.95
YN13B-04	0.282411	0.000013	0.001633	0.067098	429		0.282398	-3.79	1.21	1.65	-0.95
YN13B-05	0.282458	0.000014	0.000778	0.032196	442		0.282452	-1.61	1.12	1.52	-0.98
YN13B-06	0.282538	0.000013	0.001966	0.083138	428		0.282522	0.57	1.04	1.38	-0.94
YN13B-07	0.282436	0.000012	0.000977	0.041929	439		0.282428	-2.52	1.15	1.58	-0.97
YN13B-08	0.282404	0.000015	0.001953	0.077982	432		0.282388	-4.08	1.23	1.67	-0.94
YN13B-09	0.282134	0.000012	0.001018	0.040595	652		0.282121	-8.66	1.58	2.13	-0.97
YN13B-10	0.282466	0.000014	0.000560	0.025316	431		0.282461	-1.51	1.10	1.51	-0.98
YN13B-11	0.282474	0.000012	0.001228	0.056158	429		0.282464	-1.47	1.11	1.51	-0.96
YN13B-12	0.282310	0.000013	0.002038	0.088700	429		0.282294	-7.48	1.37	1.89	-0.94
YN13B-13	0.282458	0.000011	0.000600	0.029779	444		0.282453	-1.52	1.11	1.52	-0.98
YN13B-14	0.282453	0.000011	0.001100	0.051422	430		0.282444	-2.16	1.13	1.55	-0.97
YN13B-15	0.282469	0.000012	0.001156	0.051495	432		0.282460	-1.55	1.11	1.51	-0.97
YN13B-16	0.282397	0.000012	0.001061	0.047029	454		0.282388	-3.59	1.21	1.66	-0.97
YN13B-17	0.282499	0.000017	0.001607	0.074513	426		0.282487	-0.72	1.08	1.46	-0.95
YN13B-18	0.282469	0.000014	0.001831	0.080215	429		0.282455	-1.80	1.13	1.53	-0.94
YN13B-19	0.282514	0.000013	0.001743	0.078425	428		0.282500	-0.19	1.07	1.42	-0.95
YN13B-20	0.282480	0.000012	0.001195	0.052823	428		0.282471	-1.25	1.10	1.49	-0.96
<i>10YN-18A</i>											
YN18A-01	0.282507	0.000011	0.001771	0.077081	429		0.282493	-0.42	1.08	1.44	
YN18A-02	0.282415	0.000012	0.001134	0.050329	429		0.282406	-3.50	1.19	1.64	
YN18A-03	0.282520	0.000013	0.001733	0.075840	429		0.282506	0.04	1.06	1.41	
YN18A-04	0.282462	0.000012	0.001408	0.062133	430		0.282451	-1.92	1.13	1.54	
YN18A-05	0.282390	0.000016	0.000661	0.027909	429		0.282384	-4.29	1.21	1.68	
YN18A-06	0.282450	0.000012	0.001126	0.051515	428		0.282441	-2.31	1.14	1.56	
YN18A-07	0.282480	0.000012	0.001034	0.044549	446		0.282472	-0.81	1.09	1.48	
YN18A-08	0.282464	0.000012	0.001526	0.065678	429		0.282451	-1.91	1.13	1.53	
YN18A-09	0.282502	0.000011	0.001292	0.055266	444		0.282492	-0.15	1.07	1.43	
YN18A-10	0.282474	0.000012	0.001752	0.074223	467		0.282459	-0.81	1.12	1.49	
YN18A-11	0.282452	0.000012	0.000908	0.040740	427		0.282445	-2.18	1.13	1.55	
YN18A-12	0.282466	0.000013	0.001326	0.057079	480		0.282454	-0.67	1.12	1.49	
YN18A-13	0.282468	0.000013	0.001756	0.075275	430		0.282454	-1.80	1.13	1.53	
YN18A-14	0.282449	0.000013	0.001344	0.057001	429		0.282438	-2.36	1.15	1.56	
YN18A-15	0.282470	0.000011	0.001383	0.063053	456		0.282458	-1.08	1.12	1.50	
YN18A-16	0.282447	0.000011	0.001624	0.070519	430		0.282434	-2.48	1.16	1.57	
YN18A-17	0.282460	0.000012	0.001517	0.063652	430		0.282448	-2.00	1.14	1.54	
YN18A-18	0.282506	0.000011	0.001385	0.057239	430		0.282495	-0.36	1.07	1.44	
YN18A-19	0.282460	0.000013	0.000620	0.025906	430		0.282455	-1.75	1.11	1.53	
YN18A-20	0.282451	0.000012	0.000729	0.031578	430		0.282445	-2.12	1.13	1.55	
YN18A-21	0.282487	0.000012	0.000958	0.042296	430		0.282480	-0.90	1.08	1.47	
YN18A-22	0.282494	0.000015	0.001311	0.056052	449		0.282483	-0.34	1.08	1.45	
<i>10YN-22B</i>											
YN22B-01	0.282477	0.000010	0.002230	0.095051	430		0.282459	-1.61	1.13	1.52	-0.93
YN22B-02	0.282211	0.000011	0.001591	0.064026	429		0.282198	-10.89	1.49	2.10	-0.95
YN22B-03	0.282507	0.000012	0.001258	0.053644	427		0.282497	-0.32	1.06	1.43	-0.96
YN22B-04	0.282455	0.000009	0.001432	0.061534	429		0.282443	-2.19	1.14	1.55	-0.96
YN22B-05	0.282472	0.000012	0.000754	0.033885	431		0.282466	-1.35	1.10	1.50	-0.98
YN22B-06	0.282443	0.000012	0.001084	0.044374	490		0.282433	-1.20	1.15	1.54	-0.97
YN22B-07	0.282467	0.000012	0.000936	0.037954	428		0.282460	-1.62	1.11	1.52	-0.97
YN22B-08	0.282449	0.000011	0.000959	0.042775	428		0.282441	-2.29	1.14	1.56	-0.97
YN22B-09	0.282507	0.000011	0.001122	0.047777	428		0.282498	-0.27	1.06	1.43	-0.97
YN22B-10	0.282478	0.000013	0.000883	0.038696	428		0.282471	-1.25	1.09	1.49	-0.97
YN22B-11	0.282477	0.000013	0.000667	0.030582	430		0.282471	-1.19	1.09	1.49	-0.98
YN22B-12	0.282485	0.000013	0.001006	0.043979	453		0.282476	-0.49	1.09	1.46	-0.97
YN22B-13	0.282494	0.000011	0.001548	0.067126	429		0.282481	-0.85	1.09	1.47	-0.95
YN22B-14	0.282449	0.000013	0.002272	0.100682	428		0.282431	-2.65	1.18	1.58	-0.93
YN22B-15	0.282547	0.000013	0.001742	0.075329	429		0.282533	0.99	1.02	1.35	-0.95
YN22B-16	0.282497	0.000012	0.001083	0.047865	429		0.282488	-0.60	1.07	1.45	-0.97
YN22B-17	0.282550	0.000014	0.002517	0.106816	427		0.282530	0.83	1.04	1.36	-0.92
YN22B-18	0.282390	0.000011	0.001097	0.044384	427		0.282381	-4.45	1.22	1.69	-0.97
YN22B-19	0.282445	0.000011	0.000931	0.041863	429		0.282438	-2.38	1.14	1.56	-0.97
YN22B-20	0.282449	0.000011	0.000748	0.034704	428		0.282443	-2.25	1.13	1.55	-0.98
YN22B-21	0.282484	0.000012	0.000640	0.027782	430		0.282479	-0.90	1.08	1.47	-0.98
YN22B-22	0.282512	0.000012	0.001295	0.054780	429		0.282501	-0.14	1.06	1.42	-0.96
YN22B-23	0.282374	0.000012	0.001560	0.063893	431		0.282361	-5.07	1.26	1.74	-0.95
YN22B-24	0.282507	0.000012	0.001081	0.046053	457		0.282498	0.35	1.06	1.41	-0.97
YN22B-25	0.282403	0.000012	0.002159	0.087328	449		0.282385	-3.84	1.24	1.67	-0.93
YN22B-26	0.282494	0.000012	0.000809	0.035068	455		0.282487	-0.08	1.07	1.44	-0.98
YN22B-27	0.282439	0.000011	0.001053	0.045667	428		0.282430	-2.67	1.15	1.58	-0.97
YN22B-28	0.282489	0.000012	0.001423	0.061180	438		0.282477	-0.80	1.09	1.47	-0.96

Table 2 (continued)

Analysis	$^{176}\text{Hf}/^{177}\text{Hf}$	$\pm 1\sigma$	$^{176}\text{Lu}/^{177}\text{Hf}$	$^{176}\text{Yb}/^{177}\text{Hf}$	$^{206}\text{Pb}/^{238}\text{U}$	age (Ma)	$^{176}\text{Hf}/^{177}\text{Hf}$ (i)	$\varepsilon_{\text{Hf}}(t)$	$T_{\text{DM1}}(\text{Hf})$ (Ga)	$T_{\text{DM2}}(\text{Hf})$ (Ga)	$f_{\text{Lu/Hf}}$
YN22B-29	0.282460	0.000011	0.000811	0.035609	430		0.282454	-1.80	1.11	1.53	-0.98
YN22B-30	0.282449	0.000011	0.001255	0.052107	452		0.282439	-1.84	1.14	1.55	-0.96
10YN-22D											
YN22D-01	0.282441	0.000012	0.000603	0.027053	429		0.282436	-2.47	1.14	1.57	-0.98
YN22D-03	0.282477	0.000012	0.001297	0.054811	442		0.282466	-1.08	1.11	1.49	-0.96
YN22D-04	0.282460	0.000012	0.001359	0.059514	425		0.282449	-2.08	1.13	1.54	-0.96
YN22D-05	0.282448	0.000012	0.000590	0.027736	458		0.282443	-1.57	1.13	1.53	-0.98
YN22D-06	0.282494	0.000012	0.001041	0.045173	427		0.282486	-0.72	1.07	1.46	-0.97
YN22D-07	0.282440	0.000013	0.000966	0.040456	447		0.282432	-2.21	1.15	1.57	-0.97
YN22D-08	0.282471	0.000013	0.001118	0.048850	430		0.282462	-1.53	1.11	1.51	-0.97
YN22D-09	0.282589	0.000015	0.002019	0.086552	425		0.282573	2.31	0.97	1.26	-0.94
YN22D-10	0.282525	0.000011	0.001305	0.057004	430		0.282515	0.35	1.04	1.39	-0.96
YN22D-11	0.282481	0.000013	0.001278	0.054384	462		0.282469	-0.54	1.10	1.47	-0.96
YN22D-12	0.282468	0.000012	0.001141	0.049174	458		0.282458	-1.04	1.11	1.50	-0.97
YN22D-13	0.282489	0.000013	0.001242	0.055471	427		0.282479	-0.97	1.09	1.47	-0.96
YN22D-14	0.282404	0.000014	0.002299	0.098220	432		0.282386	-4.16	1.24	1.68	-0.93
YN22D-15	0.282493	0.000015	0.001355	0.055844	452		0.282482	-0.33	1.08	1.45	-0.96
YN22D-16	0.282502	0.000011	0.002034	0.089542	447		0.282484	-0.34	1.09	1.45	-0.94
YN22D-17	0.282425	0.000014	0.000858	0.038785	430		0.282418	-3.09	1.17	1.61	-0.97
YN22D-18	0.282431	0.000014	0.001141	0.049267	429		0.282422	-2.95	1.17	1.60	-0.97
YN22D-19	0.282446	0.000011	0.000740	0.033410	430		0.282441	-2.27	1.13	1.56	-0.98
YN22D-20	0.282458	0.000012	0.001408	0.060782	427		0.282447	-2.11	1.14	1.55	-0.96

The $^{176}\text{Hf}/^{177}\text{Hf}$ and $^{176}\text{Lu}/^{177}\text{Hf}$ ratios of chondrite and depleted mantle at the present day are 0.282772 and 0.0332, and 0.28325 and 0.0384, respectively, [Blichert-Toft and Albarede \(1997\)](#), [Griffin et al. \(2000\)](#), $\lambda = 1.865 \times 10^{-11} \text{ a}^{-1}$, [Scherer et al. \(2001\)](#). $(^{176}\text{Lu}/^{177}\text{Hf})_c = 0.015$, $t = \text{crystallization age of zircon}$.

$\varepsilon_{\text{Hf}}(t) = 10,000 \times \{[(^{176}\text{Hf}/^{177}\text{Hf})_S - (^{176}\text{Lu}/^{177}\text{Hf})_S \times (e^{2t} - 1)] / [(^{176}\text{Hf}/^{177}\text{Hf})_{\text{CHUR0}} - (^{176}\text{Lu}/^{177}\text{Hf})_{\text{CHUR}} \times (e^{2t} - 1)] - 1\}; T_{\text{DM1}}(\text{Hf}) = 1/\lambda \times \ln\{1 + [(^{176}\text{Hf}/^{177}\text{Hf})_S - (^{176}\text{Hf}/^{177}\text{Hf})_{\text{DM}}]\} / [(^{176}\text{Lu}/^{177}\text{Hf})_S - (^{176}\text{Lu}/^{177}\text{Hf})_{\text{DM}}]\}; T_{\text{DM2}}(\text{Hf}) = T_{\text{DM1}}(\text{Hf}) - (T_{\text{DM1}}(\text{Hf}) - t)(f_{\text{cc}} - f_S)/(f_{\text{cc}} - f_{\text{DM}})$, In our calculation, $f_{\text{cc}} = -0.55$ and $f_{\text{DM}} = 0.157$.

regional tectonothermal events after its emplacement, particularly during the Indosian and Cenozoic events (e.g., [Roger et al., 2000](#); [Yan et al., 2006](#); and references therein). Therefore, the geochronological framework and main emplacement time of the granitic batholith has not been well constrained so far. In the case of the granitic batholith in the Dulong area, Southwestern SCB, a preliminary emplacement age of about 390.5 Ma was inferred from whole-rock Rb-Sr isochron data ([YNBGMR, 1990](#)). [Yan et al. \(2006\)](#) obtained two precise zircon U-Pb ages of 436 ± 12 Ma and 402 ± 10 Ma, which represent the crystallization ages of the parental magmas for the mylonitic rock and granitic gneiss, respectively. Our zircon U-Pb dating on four gneissic granite samples yielded consistent crystallization ages of ~ 430 Ma ([Fig. 6a-d](#)). For the Song Chay batholith in Northern Vietnam, the preliminary investigation indicated a range of Archean to Proterozoic ages on the basis of K-Ar and U-Pb dating in the Kontum region, although no technical details were given on the dating methods used, as pointed out by [Roger et al. \(2000\)](#). A precise emplacement age of 428 ± 5 Ma was constrained subsequently by [Roger et al. \(2000\)](#). Taken together, it is clear that the granitic rocks in the Dulong-Song Chay batholith intruded mainly at ~ 430 Ma, with minor younger granitic magmatism that likely occurred at ~ 400 Ma ([Yan et al., 2006](#)).

Recent studies have documented that the 460–400 Ma granitic magmatism was intensive within the SCB, especially in the Wuyi-Yunkai orogen and the surrounding area (e.g., [Wang et al., 2007, 2011, 2012, 2013b,c](#); [Li et al., 2010](#); [Zhang et al., 2012b](#); [Chu et al., 2012a](#); [Huang et al., 2013](#); [Zhao et al., 2013](#); and references therein). In conjunction with all available dating results published previously, a peak age of ~ 430 Ma is shown in [Fig. 12](#), indicating an intense granitic magmatic event at that time. From a consideration of space-time distribution pattern, it is reasonable to infer that the Dulong-Song Chay batholith is the southwesterly extension or the products of the early Paleozoic granitic magmatism associated with the Wuyi-Yunkai orogeny in the SCB, which is also consistent with the previous proposition (e.g., [Roger et al., 2000](#); [Yan et al., 2006](#)), although it seems to be far away from the core of the orogen at present.

6.2. Magma source

As mentioned above, all the Dulong granitic rocks have high A/CNK values ($A/\text{CNK} > 1.1$; [Table 1](#) and [Fig. 8a](#)), i.e. these are strongly peraluminous and similar to S-type granites ([Fig. 8c](#); [Chappell and White, 1974, 2001](#); [Sylvester, 1998](#); [Clemens, 2003](#)). The previous studies on experimental petrology and geochemistry have documented that peraluminous granites are mainly generated by melting of crustal rocks (e.g., [Miller, 1985](#); [Petford and Atherton, 1996](#); [Sylvester, 1998](#)). Their protoliths likely include aluminum-rich metasediments (metapelites), basic meta-igneous rocks (amphibolites) and quartz-feldspathic metamorphic rocks (orthogneisses and greywackes) in the continental crust. In some cases, metaluminous meta-igneous rocks such as some orthogneisses are even able to produce peraluminous felsic melts at low melting fractions and in water-deficient conditions (e.g., [Clemens, 2003](#)). Although alternative mechanism including fractional crystallization of hornblende, was previously proposed for the development of peraluminous compositions by [Cawthorn and Brown \(1976\)](#), and [Zen \(1986\)](#) subsequently pointed out that the generation of peraluminous compositions by fractional crystallization in that way is inefficient for the large bodies of magma and that they likely reflect the nature of source region.

The Dulong granitic rocks are characterized by strong peraluminosity ($A/\text{CNK} > 1.1$), remarkably low CaO (0.31–1.66 wt.%) contents and $\text{CaO}/\text{Na}_2\text{O}$ (0.11–0.48), and high $\text{Al}_2\text{O}_3/\text{TiO}_2$ ratios (55–354) and Rb contents (152–471 ppm) ([Table 3](#)), indicating a significant contribution from an aluminum-rich pelitic source (e.g., [Chappell et al., 1991](#); [Patiño Douce, 1995](#)). This is in agreement with the suggestion of [Sylvester \(1998\)](#) who stated that S-type peraluminous melts derived from pelites have lower $\text{CaO}/\text{Na}_2\text{O}$ ratios (<0.3) than melts produced from clay-poor (greywackeous) sources. Indeed, the low CaO and Na₂O contents of the Dulong SP granitoids are similar to those of the melts produced experimentally from pelitic protoliths rather than from meta-igneous rocks ([Miller, 1985](#); [Barbero and Villaseca, 1992](#)). Moreover, the high phosphorous contents of the studied granite samples ([Fig. 9c](#)) also indicate a dominantly pelitic origin because crustal sources with the

Table 3

Major (wt%) and trace (ppm) element compositions for the Dulong granites in the western SCB.

Sample	10YN-13B	10YN-15A	10YN-16C	10YN-17D	10YN-18A	10YN-18B	10YN-19A	10YN-20B
SiO ₂	76.11	74.25	74.81	73.86	76.26	75.08	75.24	74.64
TiO ₂	0.14	0.17	0.18	0.23	0.16	0.17	0.15	0.18
Al ₂ O ₃	13.08	13.95	13.42	13.73	12.71	13.15	13.31	12.92
CaO	0.49	1.00	0.82	0.52	0.40	0.31	0.35	0.58
Fe ₂ O ₃	1.07	1.29	1.48	1.78	0.93	1.08	0.92	1.27
K ₂ O	4.16	4.07	4.00	5.05	4.92	5.83	5.29	4.98
MgO	0.32	0.35	0.41	0.53	0.28	0.39	0.27	0.67
MnO	0.02	0.04	0.04	0.04	0.02	0.02	0.03	0.04
Na ₂ O	2.88	3.55	3.26	2.37	2.79	2.58	3.06	2.52
P ₂ O ₅	0.15	0.13	0.14	0.15	0.16	0.16	0.16	0.17
L.O.I	1.02	0.61	0.87	1.18	0.78	0.65	0.66	1.46
Total	99.44	99.43	99.42	99.45	99.43	99.43	99.43	99.43
A/CNK	1.29	1.15	1.20	1.33	1.19	1.18	1.17	1.22
Sc	0.67	2.19	1.76	2.70	4.15	1.61	1.52	5.03
V	3.40	11.1	10.2	13.2	11.6	9.16	5.73	14.7
Cr	2.70	8.23	8.67	5.56	9.98	4.54	5.16	11.8
Co	0.23	1.70	1.56	2.08	1.87	0.51	0.93	2.22
Ni	0.50	4.21	2.07	1.96	9.52	1.22	1.01	2.56
Ga	5.95	15.9	12.8	16.2	20.0	11.3	9.33	21.0
Rb	152	324	319	357	455	413	228	471
Sr	14.6	48.7	41.3	42.4	30.0	49.0	17.4	23.5
Y	4.99	14.9	16.2	11.0	15.5	13.2	6.73	16.7
Zr	27.3	56.7	89.1	123.9	70.3	69.0	31.9	77.6
Nb	4.89	10.1	10.6	13.7	15.2	11.7	5.83	15.4
Cs	11.6	21.5	27.0	36.0	19.6	23.8	14.0	49.2
Ba	67.5	186	161	280	107	374	70.4	114
La	5.25	14.0	16.5	12.5	8.7	16.4	5.17	12.4
Ce	11.1	30.8	33.8	26.5	18.7	34.2	11.5	27.9
Pr	1.38	3.63	4.16	3.55	2.29	4.10	1.38	3.32
Nd	5.13	13.5	16.0	12.9	8.60	15.0	5.11	12.4
Sm	1.22	3.10	3.56	2.96	2.00	3.11	1.21	3.05
Eu	0.12	0.36	0.40	0.38	0.14	0.29	0.12	0.27
Gd	1.17	3.10	3.67	2.60	2.16	3.06	1.19	2.96
Tb	0.21	0.55	0.65	0.48	0.46	0.52	0.22	0.56
Dy	1.25	3.22	3.72	2.62	3.00	3.05	1.32	3.36
Ho	0.21	0.58	0.68	0.46	0.57	0.53	0.24	0.61
Er	0.51	1.51	1.85	1.19	1.58	1.43	0.64	1.66
Tm	0.07	0.22	0.27	0.17	0.24	0.20	0.10	0.25
Yb	0.43	1.39	1.80	1.14	1.64	1.35	0.65	1.61
Lu	0.06	0.20	0.27	0.16	0.24	0.18	0.09	0.23
Hf	1.00	1.85	3.10	3.77	2.62	2.46	1.10	2.64
Ta	0.95	1.84	2.19	3.04	3.84	2.47	1.56	4.10
Pb	10.5	27.2	27.7	23.5	19.5	18.5	14.4	20.7
Th	4.20	10.8	12.1	14.8	11.4	11.5	4.67	11.1
U	3.73	12.95	8.59	8.27	6.33	3.97	7.75	57.17

Sample	10YN-20C	10YN-20D	10YN-21A	10YN-22B	10YN-22C	10YN-22D	10YN-22E
SiO ₂	76.02	75.98	74.04	69.65	72.13	74.46	74.12
TiO ₂	0.04	0.04	0.16	0.28	0.26	0.18	0.17
Al ₂ O ₃	13.23	13.06	13.79	15.90	14.42	13.32	13.42
CaO	0.46	0.48	0.87	1.66	1.39	0.93	0.92
Fe ₂ O ₃	0.78	0.93	1.34	1.92	1.84	1.42	1.33
K ₂ O	4.87	4.80	4.84	3.91	5.09	5.40	5.41
MgO	0.10	0.11	0.34	0.83	0.56	0.41	0.40
MnO	0.02	0.02	0.04	0.04	0.04	0.03	0.04
Na ₂ O	3.14	3.16	3.17	4.27	3.00	2.41	2.66
P ₂ O ₅	0.16	0.16	0.17	0.13	0.13	0.10	0.12
L.O.I	0.61	0.67	0.66	0.84	0.57	0.74	0.85
Total	99.43	99.41	99.43	99.42	99.42	99.42	99.43
A/CNK	1.17	1.16	1.15	1.11	1.11	1.16	1.13
Sc	0.04	1.54	1.59	2.35	3.17	1.51	1.12
V	0.30	1.01	8.58	18.6	20.3	11.3	12.1
Cr	0.72	4.36	6.71	12.0	7.25	9.81	6.26
Co	0.04	0.24	1.32	1.59	3.02	1.87	1.95
Ni	0.01	1.00	1.63	2.66	4.62	5.83	2.40
Ga	5.66	18.0	13.3	14.9	16.1	13.3	11.4
Rb	187	390	399	271	323	309	298
Sr	2.89	6.45	48.1	140	90.2	66.1	57.4
Y	6.83	13.0	14.3	14.3	20.3	16.8	15.8
Zr	19.9	39.3	73.5	106	122	83.1	74.1
Nb	3.56	6.92	12.5	10.7	10.6	7.12	7.13
Cs	7.2	12.9	47.0	30.3	33.6	28.9	25.1

Table 3 (continued)

Sample	10YN-20C	10YN-20D	10YN-21A	10YN-22B	10YN-22C	10YN-22D	10YN-22E
Ba	2.21	4.20	172	301	479	187	284
La	1.43	2.88	12.2	20.0	25.6	12.3	11.9
Ce	3.13	6.23	26.7	42.6	53.3	26.1	23.8
Pr	0.40	0.79	3.14	4.99	6.50	3.31	3.00
Nd	1.42	2.66	12.0	19.0	24.5	12.5	11.5
Sm	0.53	0.98	2.90	4.07	5.23	2.77	2.67
Eu	0.01	0.03	0.36	0.58	0.68	0.32	0.37
Gd	0.70	1.22	2.92	3.93	5.05	2.76	2.99
Tb	0.20	0.36	0.57	0.63	0.84	0.51	0.53
Dy	1.47	2.63	3.42	3.53	4.51	3.21	3.29
Ho	0.28	0.49	0.62	0.60	0.81	0.65	0.66
Er	0.76	1.34	1.53	1.47	2.02	1.80	1.68
Tm	0.12	0.21	0.21	0.19	0.27	0.25	0.24
Yb	0.80	1.39	1.38	1.17	1.56	1.53	1.45
Lu	0.12	0.20	0.19	0.18	0.23	0.22	0.21
Hf	1.10	2.04	2.61	3.29	3.63	2.80	2.56
Ta	1.07	1.94	5.13	2.30	1.36	1.48	1.24
Pb	15.3	29.2	31.0	25.9	35.5	30.3	29.7
Th	3.84	9.15	9.91	14.5	16.0	14.0	13.4
U	6.31	5.84	9.88	4.24	7.04	5.01	4.34

A/CNK = (mol. Al₂O₃/(CaO + K₂O + Na₂O)), Mg# = (100 × molar MgO/(MgO + FeO), FeO = 0.8998 × Fe₂O₃.

Table 4

Sr and Nd isotopic compositions of the Dulong granites in the western SCB.

Samples	Rb	Sr	⁸⁷ Rb/ ⁸⁶ Sr	⁸⁷ Sr/ ⁸⁶ Sr (2σm)	⁸⁷ Sr/ ⁸⁶ Sr(t)	Sm	Nd	¹⁴⁷ Sm/ ¹⁴⁴ Nd	¹⁴³ Nd/ ¹⁴⁴ Nd (2σm)	¹⁴³ Nd/ ¹⁴⁴ (t)	$\varepsilon_{\text{Nd}}(t)$	T _{DM2} (Ga)
10YN-17D	357	42.4	24.7	0.868341 (12)	0.71688	2.96	12.90	0.1384	0.512146 (4)	0.511756	-6.4	1.69
10YN-18A	455	30.0	45.1	0.990894 (9)	0.71486	2.00	8.60	0.1406	0.512140 (4)	0.511744	-6.6	1.7
10YN-19A	228	17.4	38.9	0.984095 (9)	0.74594	1.21	5.11	0.1431	0.512136 (6)	0.511732	-6.9	1.72
10YN-22B	271	140	5.6	0.752914 (6)	0.71855	4.07	19.00	0.1297	0.512130 (6)	0.511765	-6.2	1.67
10YN-22D	309	66.1	13.7	0.805508 (5)	0.72190	2.77	12.50	0.1344	0.512141 (4)	0.511763	-6.3	1.67
10YN-13B						1.22	5.13	0.1438	0.512118 (6)	0.511713	-7.2	1.75
10YN-20C						0.53	1.42	0.2261	0.512346 (9)	0.511709	-7.3	1.83

Notions: Chondrite uniform reservoir values, ¹⁴⁷Sm/¹⁴⁴Nd = 0.1967, ¹⁴³Nd/¹⁴⁴Nd = 0.512638, were used for the calculation. T_{DM1} values were calculated based on present-day (¹⁴⁷Sm/¹⁴⁴Nd)_{DM} = 0.2137 and (¹⁴³Nd/¹⁴⁴Nd)_{DM} = 0.51315. Sm and Nd in ppm. T_{DM1} = $1/\lambda \times \ln(1 + [(^{143}\text{Nd}/^{144}\text{Nd})_s - 0.51315]/[(^{147}\text{Sm}/^{144}\text{Nd})_s - 0.2137])$; T_{DM2} = T_{DM1} - (T_{DM1} - t) × ((f_{cc} - f_s)/(f_{cc} - f_{DM})); where s = sample, f_{cc}, f_s and f_{DM} are the f_{Sm} = Nd values of the continental crust, the sample and the depleted mantle, respectively. In our calculation, f_{cc} = -0.4 and f_{DM} = 0.08592; where t = 430 Ma.

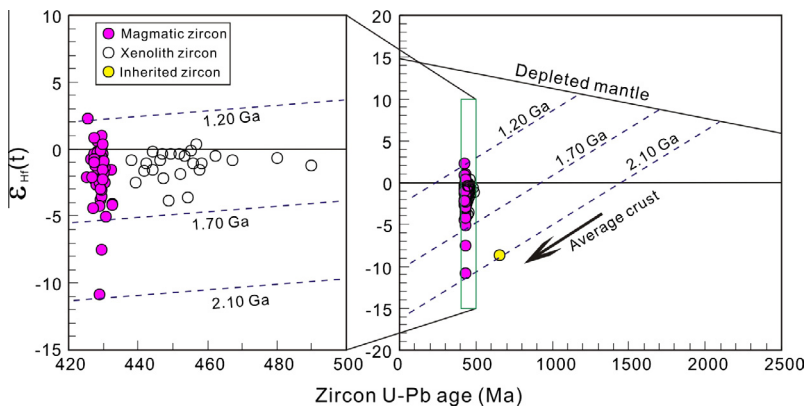


Fig. 7. Relationship between $\varepsilon_{\text{Hf}}(t)$ values and U-Pb ages for zircons from the Dulong granitic rocks. Hf isotopic compositions of chondrite and depleted mantle are from Blichert-Toft and Albarede (1997) and Vervoort and Blichert-Toft (1999).

highest phosphorous enrichments are pelitic shales (e.g., Gromet et al., 1984) and apatite is more soluble in highly peraluminous melts (e.g., Bea et al., 1992; Wolf and London, 1994). In the Rb/Ba vs. Rb/Sr diagram (Fig. 13), most of the Dulong granite samples plot within the Himalayan strongly peraluminous granites, demonstrating a clay-rich source and a low plagioclase content (Chappell and White, 1992; Sylvester, 1998). Obviously, a dominant origin from the partial melting of aluminum-rich pelitic rocks is the most plausible to account for their geochemical signatures. Furthermore, both major and trace element compositions indicate that the

Dulong granitic rocks have high Rb/Sr ratio (Fig. 13), Al₂O₃ content (Table 3), and K₂O/Na₂O value (>1), comparable with compositions obtained for experimental melts from melting of biotite-rich pelitic sources (Patiño Douce and Harris, 1998).

The relatively flat HREE patterns of all the Dulong granites (Fig. 10a), with (Gd/Yb)_N values in the range of 0.9–3.1, suggest the absence of fractional crystallization of garnet in their magma source and, therefore, middle/upper crustal levels of partial melting. This feature is also common to most SP granites (e.g., Rossi et al., 2002). Accordingly, the protoliths of metasedimentary source

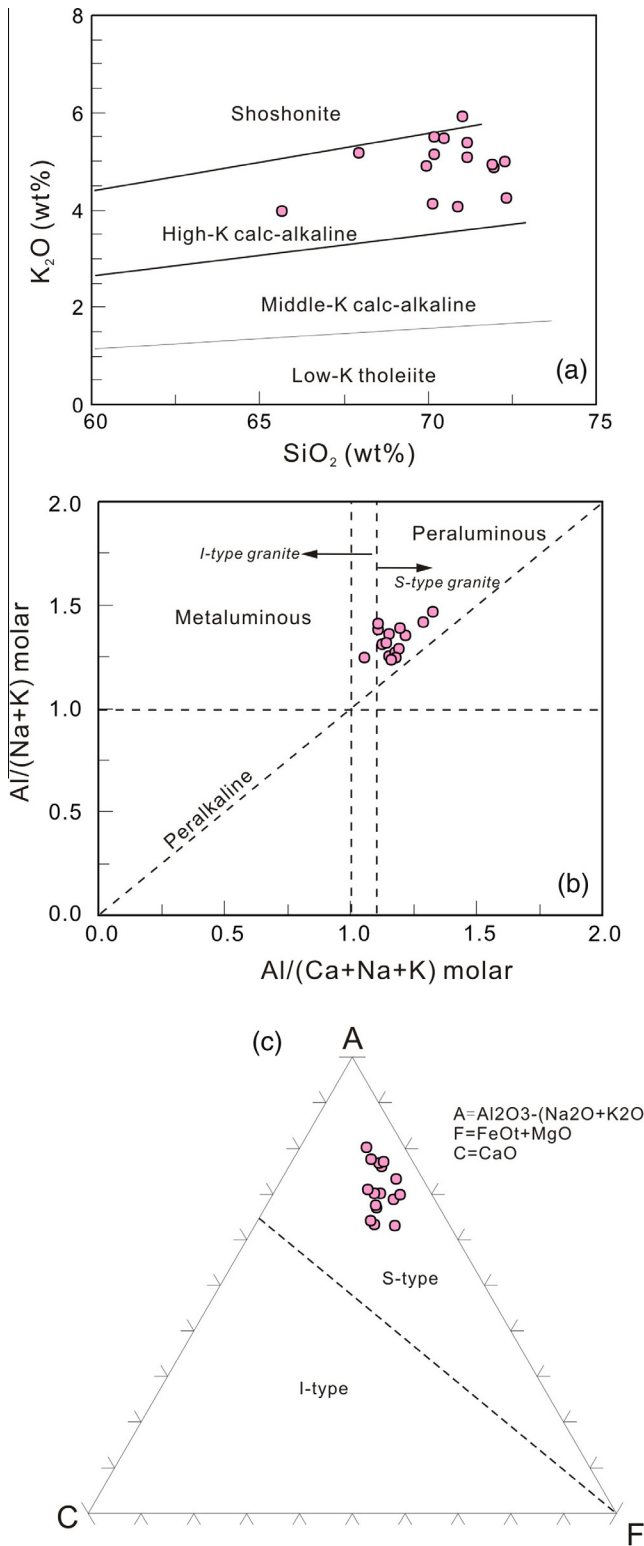


Fig. 8. (a) K_2O versus SiO_2 (after Winchester and Floyd, 1977), (b) Molar $Al/(K + Na)$ versus $Al/(Ca + Na + K)$ diagram, and (c) ACF diagram (after Chappell and White, 1992). Whole rock compositions are corrected for loss-on-ignition.

for the parental magma of the Dulong granitoids was in the middle/upper crust, likely corresponding to the Proterozoic or early Paleozoic sedimentary rocks in the SCB (e.g., Li and McCulloch, 1996; Shen et al., 2009). By further comparison, the $\varepsilon_{Nd}(t = 430 \text{ Ma})$ values of the Dulong granitic rocks (between -7.32 and -6.23) are higher than those of the Cambrian to Ordovician sediments

($\varepsilon_{Nd}(t = 430 \text{ Ma})$ with values ranging from -8.34 to -14.94 , Shen et al., 2009) in the SCB, which indicates that the parental magma could not have been derived directly from the partial melting of the early Paleozoic sedimentary rocks. In fact, the early Paleozoic sedimentary rocks that are dominated by psammites with very minor interlayered shales in the SCB (Li and McCulloch, 1996; Shen et al., 2009), cannot produce such strongly peraluminous melts (e.g., Patiño Douce, 1995; Sylvester, 1998), like the Dulong granitic rocks. Furthermore, based on the previous investigation (e.g., YNBGMR, 1990), the Cambrian to Ordovician sediments in the western SCB, especially in the Dulong area, are dominated by limestones with minor intercalated shales and siltstones (YNBGMR, 1976), which are unlikely the protoliths for generating the Dulong granitic magmas. Accordingly, the origin of the Dulong granitic rocks by partial melting of the early Paleozoic sediments can be ruled out. In contrast, the Neoproterozoic sedimentary sequences such as the Banxi and Danzhou groups that are dominated by pelitic rocks with minor intercalated siltstones with a total thickness up to 10 km in the SCB (e.g., Shen et al., 1993, 2009; Li and McCulloch, 1996; Chen and Jahn, 1998), are the most likely source for generating strongly peraluminous magmas with a large volume as the early Paleozoic granitic rocks exposed in the SCB (e.g., Wang et al., 2007, 2011; Zhang et al., 2012b). Their higher $\varepsilon_{Nd}(t = 430 \text{ Ma})$ values than those of the Proterozoic sedimentary rocks in the SCB (Fig. 11b; Li and McCulloch, 1996; Chen and Jahn, 1998) suggest that a single origin by partial melting of the Proterozoic sedimentary rocks is unlikely responsible for the Nd isotopic compositions of the Dulong granitic rocks. Hence, a mantle-derived basic source could also have been involved in the petrogenesis of the Dulong granitic rocks.

6.3. Magma mixing between crust- and mantle-derived melts

Taken into account the lower closure temperature in the Sm–Nd isotopic system than the Lu–Hf system in zircons (e.g., Gruau et al., 1996) whole-rock Nd isotopic compositions generally reflect the end-product of magma formation and mixing and, therefore, may mask details of key petrogenetic processes. Hence, the Nd isotopic compositions tend to be homogenous for mixed magmas (e.g., Griffin et al., 2002). In contrast, the Hf-in-zircon isotopic data have the potential to provide insights into the sequence of processes generating S-type granitoids (e.g., Belousova et al., 2006; Kemp et al., 2007; Phillips et al., 2011). The zircon Hf isotopic compositions (particularly some zircon grains with $\varepsilon_{Hf}(t = 430) > 0$; Table 2 and Fig. 7) of the Dulong granitic rocks distinctly indicate some additional input of mantle- or juvenile crust-derived magma in their genesis (e.g., Griffin et al., 2002; Belousova et al., 2006). It is therefore noticeable that the Dulong granitic rocks do not represent a single melt of pure crustal melting, but a hybrid of crust- and mantle-derived magmas. Indeed, as a result of the pioneering work of Griffin et al. (2002), similar studies of zircon Hf isotopes from different granitic rocks worldwide, have documented that mixing between mantle- and juvenile crust-derived magmas may have played a crucial role in the genesis of many peraluminous and even strongly peraluminous granitoids (e.g., Belousova et al., 2006; Kemp et al., 2007; Chen et al., 2013; Liu et al., 2013). Also, a magma mixing origin for peraluminous granites is more compatible with the presence of mafic enclaves in S-type granites of the LFB (e.g., Vernon et al., 1988; Elburg, 1996; Waight et al., 2001), and with other petrological studies of S-type granites from elsewhere in the world (e.g., Garcia et al., 1994; Sandeman and Clarke, 2003), and even with experimental studies (Patiño Douce, 1995). A wide variation in Hf isotopic compositions in the Dulong granites might have been caused either by insufficient mixing during the melting process or by heterogeneous contamination (e.g., Zheng et al., 2007).

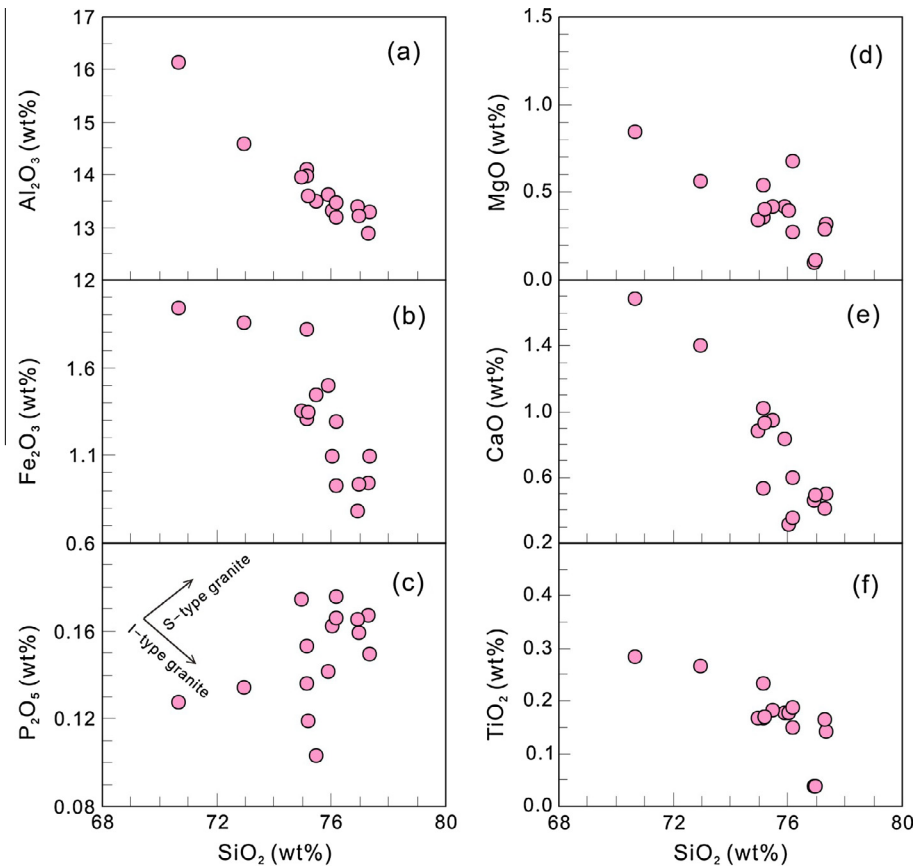


Fig. 9. Harker variation diagrams for the Dulong granitic rocks.

Although some synchronous mantle-derived mafic rocks have been identified recently in the SCB, such as high-Mg basalts (Yao et al., 2012) and mafic intrusions (Wang et al., 2013c), the former have markedly lower whole-rock Nd isotopic compositions with $\varepsilon_{\text{Nd}}(t)$ values ranging from -8.4 to -8.0 (Yao et al., 2012) than the Dulong granitic rocks with $\varepsilon_{\text{Nd}}(t)$ values of -7.32 to -6.23 (Table 4), indicating that the magma mixing between those basaltic magmas and crust-derived felsic melts could not produce the Dulong granitic parental magma. In the case of the latter, modeling results based on whole-rock Nd isotopic data demonstrate that the input of mantle-derived magma (despite the least contaminated sample with $\varepsilon_{\text{Nd}}(t)$ value of -0.7 , Wang et al., 2013c) into the crust-derived felsic magma would be more than 50% in volume to account for the Nd isotopic compositions of the Dulong granitic rocks (Fig. 14). Such a high mantle contribution does not seem to be realistic to generate the strongly peraluminous nature in the resultant magma (e.g., Collins, 1998), like the Dulong granitic rocks. Consequently, an alternative mafic endmember from a more depleted mantle was likely involved in their genesis. Actually, a more depleted mantle has recently been revealed in the Wuyi-Yunkai area by Zhang et al. (2012a), particularly like the Xinyi metabasalt with $\varepsilon_{\text{Nd}}(430 \text{ Ma}) = 3.85$ in the northern Yunkai Domain. Further modeling results (Fig. 14) show that the addition of mantle-derived magma with a volume of <20% into the crust-derived melt would be more plausible to explain the elemental and isotopic signatures for the Dulong granitic rocks, and even all early Paleozoic strongly peraluminous granitoids in the SCB (e.g., Wang et al., 2011; Zhang et al., 2012b). Our proposition is also coupled with the new results for the early Paleozoic granites within the core of the Wuyi-Yunkai orogen zone from Xia et al.

(2014). Therefore, it is likely that a large volume of mantle-derived mafic magmas that are more depleted than the recognized basic rocks (e.g., Yao et al., 2012; Wang et al., 2013c) were beneath the in the SCB.

The high SiO₂ contents (most of them greater than about 75 wt.% on a volatile-free basis, Table 3) of the Dulong granitic rocks indicate that magma mixing preceded the final emplacement of the magmas and took place in deeper magma chambers (e.g., Barbarin and Didier, 1992; Griffin et al., 2002), and that extensive fractional crystallization processes could occur during the evolution and emplacement of these hybrid magmas into their present situation (e.g., Collins, 1996; Wu et al., 2003; Qiu et al., 2008). Indeed, the decrease of CaO, FeOt, MgO, TiO₂, and Al₂O₃ with increasing SiO₂ (Fig. 9a-f) and the strong negative Eu, Ba, Nb, Tb, Sr, P and Ti anomalies (Fig. 10a and b) are also in support of fractional crystallization during magmatic evolution, including feldspar, K-feldspar, biotite and accessory mineral fractionation. On Fig. 15, it is clear that the fractional crystallization of plagioclase, K-feldspar and biotite occurred during magmatic evolution. Moreover, extreme fractionation of K-feldspar, plagioclase, quartz and biotite can explain the major element compositions and the strong negative Eu anomaly in some samples.

6.4. Tectonic setting

As discussed before, the Dulong granitic rocks can be the south-westerly extension of the early Paleozoic Wuyi-Yunkai granitoids. They should therefore be generated in the same tectonic setting. Nonetheless, whether the early Paleozoic magmatism, especially for the 460–400 Ma granitic magmatism in the whole SCB, is

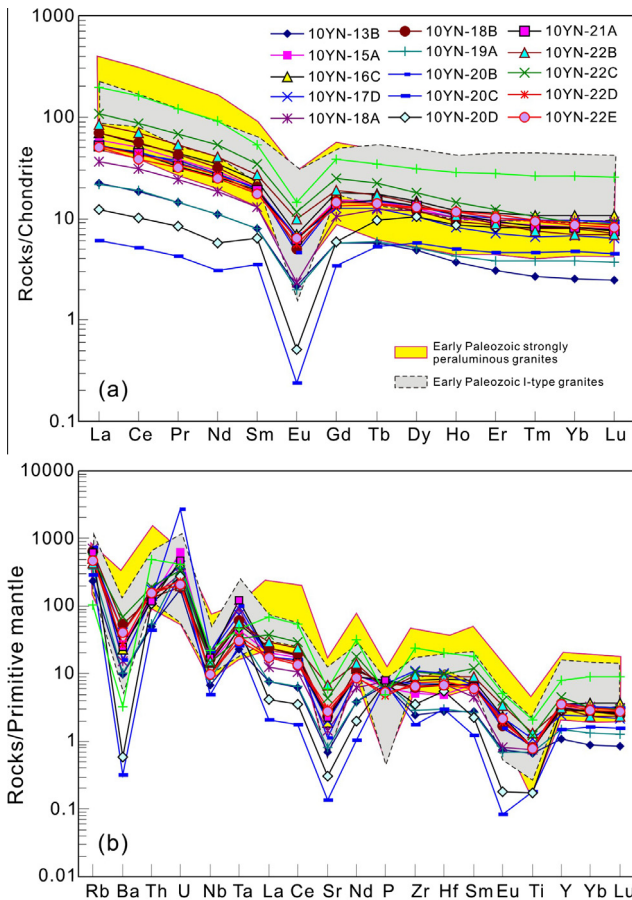


Fig. 10. (a) Chondrite-normalized REE patterns and (b) primitive mantle-normalized spider diagrams for the Dulong granitic rocks. Normalizing values of chondrite and primitive mantle are from Taylor and McLennan (1985) and Sun and McDonough (1989), respectively. The early Paleozoic strongly peraluminous granites are from Wang et al. (2011) and Zhang et al. (2012b); and the early Paleozoic I-type granites are from Huang et al. (2013) and Zhao et al. (2013).

the consequence of the syncollision/synorogen or postcollision/postorogen, remains controversial so far. For example, Yan et al. (2006) and Wang et al. (2013d) considered these granitic rocks to be the result of crustal anatexis during crustal shortening and thickening corresponding to synorogenic stage. In contrast, most workers (e.g., Li et al., 2010; Wang et al., 2011, 2013b,c; Zhang et al., 2012b; Huang et al., 2013; Zhao et al., 2013) believed that only those granitic rocks younger than ~430 Ma were generated in a postorogenic setting.

Although radiogenic decay of heat-producing elements (K, U, Th) at depth (e.g., Thompson and Connolly, 1995; Searle et al., 1997) or crustal doubling by thrusting or thickening (e.g., Patiño Douce and Harris, 1998; Nabelek and Liu, 1999) during orogenic process is potentially able to produce granitic melts, they are migmatites and low volumes of nearly in-situ wet leucogranites in general (e.g., England and Thompson, 1984; Stevens and Clemens, 1993). Accordingly, it fails to provide sufficient heat to generate such large volumes of granitic melt as the early Paleozoic granitic rocks exposed widely in the SCB (Fig. 1). In fact, an increasing number of studies have documented that the majority of collision-related, strongly peraluminous granites in various orogens are best described as ‘post-collisional’ after the climax of crustal thickening, such as in the European Alps (e.g., Altherr et al., 1995), the Caledonides (e.g., Searle et al., 1997), the Hercynides (e.g., Finger et al., 1997), the Lachlan Fold Belt (e.g., Allen et al., 1998; Villaseca et al., 1998a,b) and the Andean margins (e.g., Atherton, 1990). Their generation has been ascribed to enhanced heat flux

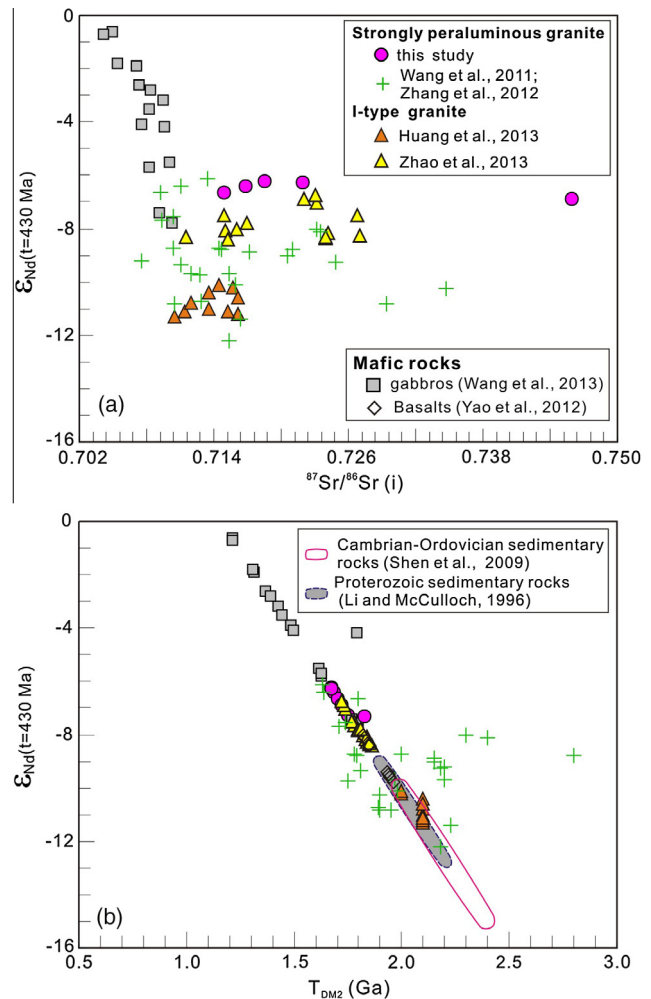


Fig. 11. $\varepsilon_{\text{Nd}}(t)$ versus (a) initial $^{87}\text{Sr}/^{86}\text{Sr}(t)$ ($t = 430$ Ma) and (b) $T_{\text{DM}2}$. Data sources: Precambrian sediments at the southern margin of Yangtze Block from Li and McCulloch (1996).

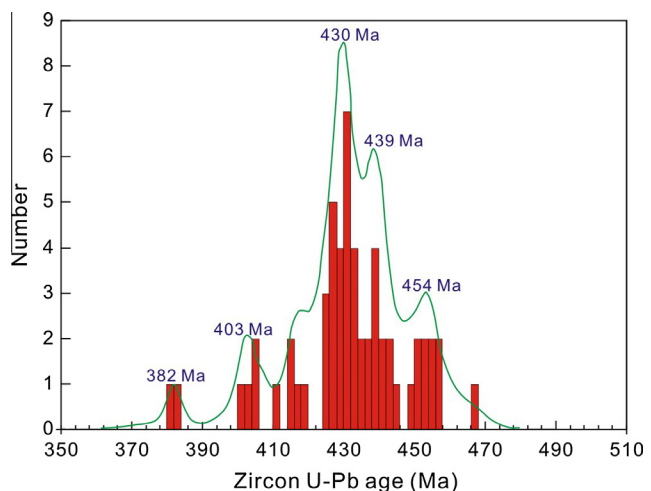


Fig. 12. Geochronology histogram showing the age range of the early Paleozoic granitoid rocks in the South China Block. Age data are based on the literatures (Chen et al., 2008; Li et al., 2010; Shen et al., 2008; Wan et al., 2010; Wang et al., 2007, 2011, 2013d; Chu et al., 2012a; Zhang et al., 2012b; Zhao et al., 2013; Huang et al., 2013).

from mantle upwelling related to post-collision or post-orogenic crustal thinning (e.g., Clemens, 2003; Kohút and Nabelek, 2008).

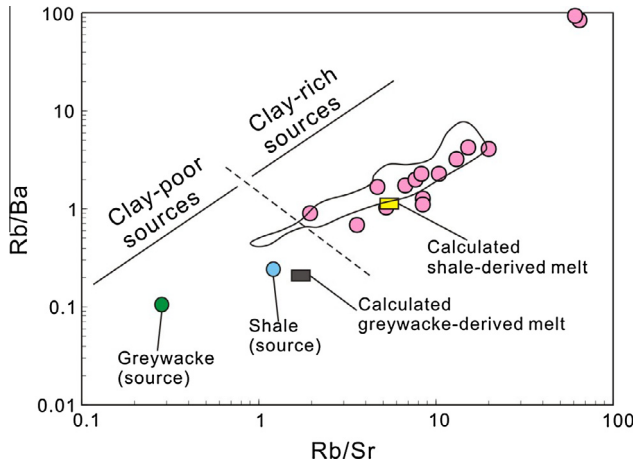


Fig. 13. Rb/Ba versus Rb/Sr diagram. Fields of the Himalayan strongly peraluminous granites are from Patiño Douce and Harris (1998). The calculated shale- and greywacke-derived melts are from Sylvester (1998). Symbols as in Fig. 7.

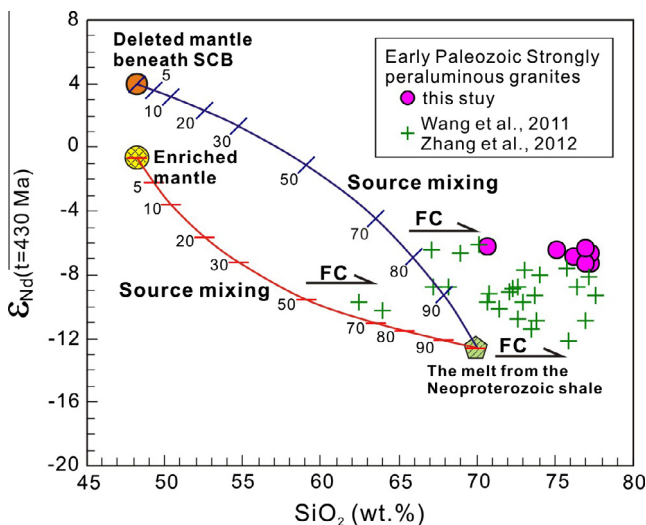


Fig. 14. SiO_2 versus $\varepsilon_{\text{Nd}}(t=430 \text{ Ma})$ diagram for the Dulong granitic rocks. The curves represent the mixing proportion between two components. The mixing parameters used for the depleted mantle is represented by $\text{SiO}_2 = 47.88 \text{ wt.\%}$, $\text{Nd} = 17.73 \text{ ppm}$, and $\varepsilon_{\text{Nd}}(t=430 \text{ Ma}) = +3.85$ (Zhang et al., 2012a). The enriched mantle that is the early Paleozoic gabbro is characterized by $\text{SiO}_2 = 48.15 \text{ wt.\%}$, $\text{Nd} = 2.7 \text{ ppm}$, and $\varepsilon_{\text{Nd}}(t=430 \text{ Ma}) = -0.7$ (Wang et al., 2013c). The melt derived from the Neoproterozoic shale has $\text{SiO}_2 = 70 \text{ wt.\%}$, $\text{Nd} = 7.8 \text{ ppm}$, and $\varepsilon_{\text{Nd}}(t=430 \text{ Ma}) = -12.67$ (Li and McCulloch, 1996).

In connection with the following several lines of evidence, it is thus obvious that an extensional regime corresponding to the postcollisional stage was responsible for the generation of the post-435 Ma magmatism in the SCB.

- (1) The recent identification of ~435 Ma high-Mg basalts in the Wuyi–Yunkai orogen revealed a potential temperature of mantle melting over 1300 °C at that time (Yao et al., 2012), which is inconsistent with a synorogenic compressional regime.
- (2) The exposure pattern of the early Paleozoic granitoids with a planar-shape spatial distribution within the SCB (Fig. 1) is incompatible with the feature of syncollisional magmatism that generally displays a linear distribution.
- (3) The mafic intrusive rocks that were generated by decompression mantle melting during lithospheric extension (i.e., ~435 Ma gabbros and diabases; Wang et al., 2013c),

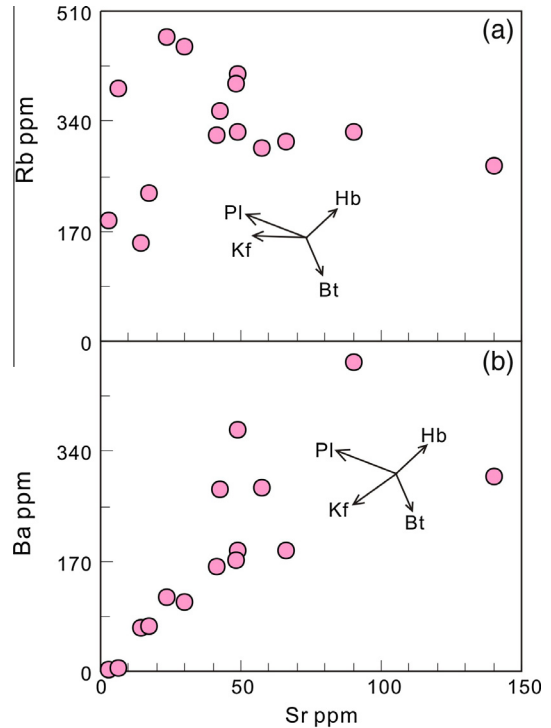


Fig. 15. Rb (a) and Ba (b) versus Sr diagrams for the Dulong granitic rocks. Kf, Pl, Bi and Hb note the removal of K-feldspar, plagioclase, biotite and hornblende during magma evolution, respectively.

together with those coeval granitoids (e.g., Li et al., 2010; Wang et al., 2011, 2013b; Zhang et al., 2012b; Huang et al., 2013; Zhao et al., 2013) within the SCB, display a bimodal pattern, which is in accord with the general signature of postcollisional extension-related magmatism (e.g., Turner et al., 1992; Li et al., 2014), rather than a compressional regime.

- (4) The recent studies on the high-grade metamorphism and deformation revealed a prograde metamorphism similar to the synorogenic crustal thickening and a retrograde metamorphism akin to the postorogenic rapid exhumation at ~460–430 Ma and at ~430–400 Ma, respectively (e.g., Li et al., 2010; Wan et al., 2010; Zhao et al., 2013; Wang et al., 2013b).

Collectively, it is well established that the ~460–435 Ma and ~435–400 Ma magmatism within the SCB corresponded to syncollisional orogen and postcollisional extension, respectively. That is, the ~435 Ma could be the key transition time of tectonic regime from syncollisional compression to postcollisional extension within the SCB.

6.5. Geodynamic model

There is a general consensus that the orogenic collapse is the key mechanism to trigger the post-collisional extension and related magmatism and metamorphism within the SCB (e.g., Li et al., 2010; Wang et al., 2007, 2011, 2013b,c; Zhang et al., 2012b; Huang et al., 2013; Zhao et al., 2013). Nevertheless, two contrasting tectonic scenarios have been invoked to account for the cause of upwelling of the asthenosphere that would perturb the original thermal gradient and that lead to large volumes of magma generation and lithospheric extension (e.g., Li et al., 2010; Wang et al., 2011, 2013b,c; Yao et al., 2012; Zhang et al.,

2012b; Huang et al., 2013). Therein, Li and coworkers (Li et al., 2010; Yao et al., 2012) proposed a delamination model of orogenic root (including lower crust and lithospheric mantle) to explain the postcollisional magmatism (especially for the generation of high-Mg basalts) and metamorphism. In contrast, based on the occurrence of the ~435 Ma gabbros and diabases in the Wuyi–Yunkai orogen, Wang et al. (2013c) believed that the lithospheric mantle delamination without involving lower crust together was responsible for the post-435 Ma magmatism and metamorphism.

Although the delamination of the eclogitized lower crust is an important process for the evolution of many orogens (e.g., Wang et al., 2006a; Krystopowicz and Currie, 2013; and references therein), it generally results in the generation of some adakite-like magmas with high La/Yb ratios that are derived from partial melting of eclogitized lower crust or its corresponding founded segment due to the high potential temperature from upwelling asthenosphere (e.g., Wang et al., 2006a; Zhang et al., 2007). However, such igneous rocks have not been observed within the entire SCB to date; instead, minor I-type granitoids (~436 Ma) that were probably derived from partial melting of ancient lower crust are present in the Taishan area (Huang et al., 2013). On the other hand, the delamination of the lower crust would accompany the delamination of the underlying lithospheric root with it and lead to the replacement of an old enriched mantle progressively by asthenosphere (Perry et al., 1988). In this case, the underlying old and enriched lithospheric mantle modified by subduction-related fluids/melts during Neoproterozoic time would be founded down into the asthenospheric mantle with the eclogitized lower crust. In fact, the studies on the early Mesozoic mafic igneous rocks from the two sides of the Jiangshan–Shaoxing zone, even the Wuyi–Yunkai orogenic domain (e.g., Wang, 2004; Wang et al., 2003, 2008) have revealed that such an enriched mantle had been preserved till at least early Mesozoic. Taking into account the absence of slab subduction within the SCB since the Neoproterozoic amalgamation between the Yangtze and Cathaysia blocks (e.g., Li and Li, 2007; Wang et al., 2008, 2012; Chu et al., 2012b), such enriched mantle had not been removed completely during the Wuyi–Yunkai orogeny, at least partially preserved beneath the Wuyi–Yunkai orogen.

The model of lower crust delamination has, therefore, difficulties to explain the origin of early Mesozoic mafic rocks that were derived from partial fusion of subduction-related enriched mantle within the SCB. On the contrary, partial delamination of overthickened lithospheric root without lower crust (e.g., Gvirtzman, 2002) is the most feasible mechanism to account for the aforementioned observation. Such a scenario is in good agreement with the recent proposition for the genesis of the ~435 Ma gabbros and diabases within the SCB (Wang et al., 2013c). Indeed, similar observations have been used to infer lithosphere removal in other mountain belts, such as the Tibetan Plateau (e.g., England and Houseman, 1989; Jiménez-Munt et al., 2008), East Anatolian Plateau (e.g., Keskin, 2003; Sengör et al., 2003), Eastern Carpathians (e.g., Knapp et al., 2005; Fillerup et al., 2010), Adirondack Mountains (e.g., McLellan et al., 2010), Sierra–Nevada region (e.g., Ducea and Saleeby, 1998), and Variscan orogen (e.g., Gutiérrez-Alonso et al., 2011), suggesting that this is an important process in orogen evolution.

In combination with the above discussion, we propose a new lithospheric delamination model that is slightly different from Wang's model (Wang et al., 2013c) to account for the early Paleozoic magmatism (Fig. 16). At the syncollisional stage (~460–435 Ma), the crust in the Wuyi–Yunkai area was strongly shortened and thickened, which resulted in high-T crustal anatexis and the generation of the granites (Fig. 16a), such as those gneissic granites of ~460–435 Ma (e.g., Wang et al., 2007, 2011; Li et al., 2010; Zhang et al., 2012b). Meanwhile, the shortening of the upper crust would be accompanied by thickening of the deeper lithosphere, which ultimately led to an overthickened lithospheric root (Fig. 16a; Turner et al., 1992; Platt and England, 1994). Such lithospheric root was denser than the underlying asthenosphere, part of which would then be removed either by mechanical delamination or by convective removal of the thermal boundary-layer (Fig. 16b; Turner et al., 1992; Platt and England, 1994). The lithosphere delamination would in turn cause the upwelling of the asthenosphere, which provided the heat needed to trigger melting of the remnants of the heterogeneous enriched mantle wedge and the depleted lithospheric mantle (e.g., Gvirtzman, 2002; Gutiérrez-Alonso et al., 2011).

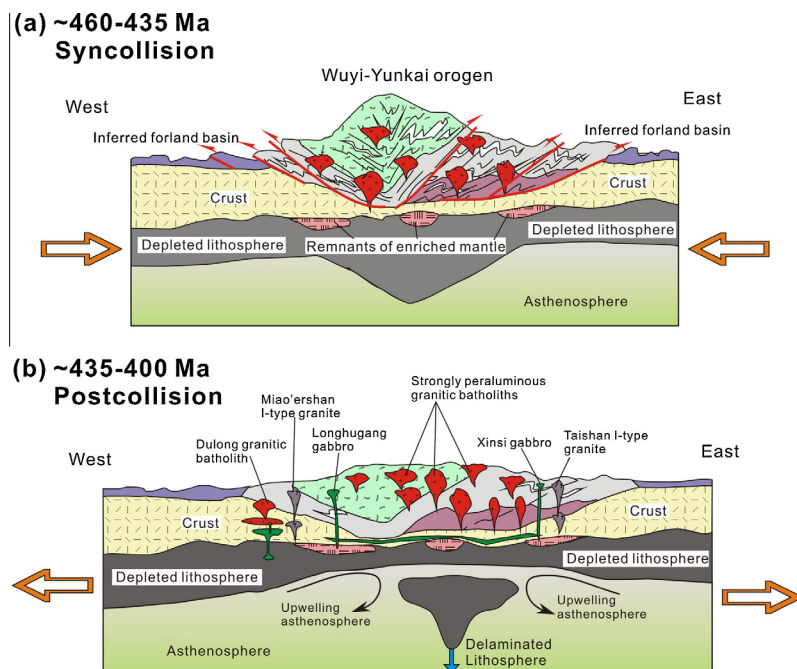


Fig. 16. Cartoons showing the geodynamic setting (modified after Wang et al. (2013d)) and petrogenetic model for the Dulong granitic rocks and other associated magmatism. See texts for more details. (a) At ~460–435 Ma, corresponding to the syn-collisional stage; and (b) At ~435–400 Ma, in response to post-orogenic extensional collapse.

As a consequence, partial fusion of the relic enriched lithospheric mantle veins with heterogeneous isotopic compositions produced the ~435 Ma mafic igneous rocks as observed in the Longhugang, Xinsi and Chayuansha areas (Fig. 16b; Wang et al., 2013c; Yao et al., 2012). On the other hand, partial melting of the depleted lithospheric mantle would generate large volumes of basic magma; these magmas would then intrude into the middle/upper crust to form a large magma chamber. This high-T magma would promote massive crustal melting to produce voluminous granitic melts (e.g., Gvirtzman, 2002; Gutiérrez-Alonso et al., 2011). Meanwhile, the minor input of depleted mantle-derived materials into the granitic parental magma would result in the generation of some strongly peraluminous granites, such as those in the Wuyi–Yunkai orogen, in particularly the Dulong batholith (Fig. 16b). The onset of mafic magmas and massive crustal melting marked the occurrence of orogenic collapse and post-collisional extension at that time (Gvirtzman, 2002; Gutiérrez-Alonso et al., 2011).

No exposure of early Paleozoic more depleted basic rocks than the Longhugang, Xinsi and Chayuansha mafic rocks (Wang et al., 2013c; Yao et al., 2012) on the surface in the SCB is likely due to the fact that the depleted mantle was devoid of water and refractory, and that the crust was overthickened. In this respect, the mafic magma derived from such mantle would be more viscous than those from the enriched lithospheric mantle; this was not easy to transport upwards and eventually was emplaced at depth. In contrast, the mafic magma derived from the enriched lithospheric mantle was rich in water, which was prone to intrude into higher crustal level, and even some erupted to the surface, such as the gabbros and diabases in the Longhugang and Xinsi areas (Wang et al., 2013c), and the high-Mg basalts in the Chayuanshan (Yao et al., 2012) (Fig. 16b). Such a scenario is the most viable to explain the early Paleozoic magmatism and related metamorphism observed in the SCB.

7. Conclusions

Geochronological, geochemical, and whole-rock Nd and zircon Hf isotopic data for the early Paleozoic granites in the southeastern Yunnan, SW China, along with regional data in the SCB, allow us to reach the following conclusions:

- (1) The gneissic granites in the Dulong batholith were emplaced mainly at ~430 Ma and display a strongly peraluminous nature.
- (2) The Dulong granitic rocks originated dominantly from partial melting of the Neoproterozoic sediments dominated by pelitic rocks with minor interlayered siltstones, and few proportions of the depleted mantle-derived melts have also been involved in their genesis.
- (3) The post-orogenic extensional collapse related to partial delamination of overthickened lithospheric mantle root without lower crust is responsible for the post-435 Ma magmatism in the SCB.

Acknowledgements

We wish to acknowledge H.-C. Liu and Y.-F. Cai for their help during the fieldwork, and Y. Liu for their skillful assistance during geochemical analyses, and Dr. L. Li for help with LA-ICP-MS dating. The authors also want to thank two anonymous reviewers for their constructive comments that helped improving our manuscript. This research received financial support from the Natural Science Foundation of China (Grant nos. 41172095, 41190070, 41190073, 41272126 and 40972046). This is a contribution from the Guang-

zhou Institute of Geochemistry, Chinese Academy of Sciences (GIG, CAS; No. 1993).

References

- Altherr, R., Lugovic, B., Meyer, H.-P., Majer, V., 1995. Early Miocene post-collisional calc-alkaline magmatism along the easternmost segment of the Periadriatic fault system (Slovenia and Croatia). *Mineral. Petrol.* 54, 225–247.
- Anderson, T., 2002. Correction of common lead in U-Pb analyses that do not report 204Pb. *Chem. Geol.* 192, 59–79.
- Atherton, M.P., 1990. The Coastal Batholith of Peru: the product of rapid recycling of 'new' crust formed within rifted continental margin. *Geol. J.* 25, 337–350.
- Barbarin, B., Didier, J., 1992. Genesis and evolution of mafic microgranular enclaves through various types of interaction between coexisting felsic and mafic magmas. *Trans. Roy. Soc. Edinb.: Earth Sci.* 83, 145–153.
- Barbero, I., Villaseca, C., 1992. The Layos granite, Hercynian complex of Toledo (Spain): an example of paraautochthonous restite-rich granite in a granulitic area. *Trans. Roy. Soc. Edinb.: Earth Sci.* 83, 127–138.
- Bea, F., Fershtater, G., Corretgé, L.G., 1992. The geochemistry of phosphorus in granite rocks and the effect of aluminium. *Lithos* 29, 43–56.
- Belousov, E.A., Griffin, W.L., O'Reilly, S.Y., 2006. Zircon crystal morphology, trace element signatures and Hf isotope composition as a tool for petrogenetic modelling: examples from eastern Australian granitoids. *J. Petrol.* 47, 329–353.
- Blichert-Toft, J., Albarede, F., 1997. The Lu-Hf geochemistry of chondrites and the evolution of the mantle–crust system. *Earth Planet. Sci. Lett.* 148, 243–258.
- Cawthorn, R.G., Brown, P.A., 1976. A model for the formation and crystallization of corundum-normative calc-alkaline magmas through amphibole fractionation. *J. Geol.* 84, 467–476.
- Chappell, B.W., 1999. Aluminium saturation in I- and S-type granites and the characterization of fractionated haplogranites. *Lithos* 46, 535–551.
- Chappell, B.W., White, A.J.R., 1974. Two contrasting granite types. *Pac. Geol.* 8, 173–179.
- Chappell, B.W., White, A.J.R., 1992. I- and S-type granites in Lachlan Fold Belt. *Trans. Roy. Soc. Edinb.* 83, 1–26.
- Chappell, B.W., White, A.J.R., 2001. Two contrasting granite types: 25 years later. *Aust. J. Earth Sci.* 48, 488–489.
- Chappell, B.W., White, A.J.R., Williams, I.S., 1991. A transverse section through granites of the Lachlan Fold Belt. In: Second Hutton Symposium Excursion Guide. ABMR Record 1991/22, Canberra, pp 1–125.
- Charvet, J., Shu, L.S., Shi, Y.S., Guo, L.Z., Faure, M., 1996. The building of south China: collision of Yangtze and Cathaysia blocks, problems and tentative answers. *J. SE Asian Earth Sci.* 13, 223–235.
- Charvet, J., Shu, L.S., Faure, M., Choulet, F., Wang, B., Lu, H.F., Breton, N.L., 2010. Structural development of the Lower Paleozoic belt of South China: genesis of an intracontinental orogen. *J. Asian Earth Sci.* 39, 309–330.
- Chen, J.F., Jahn, B.M., 1998. Crustal evolution of southeastern China: Nd and Sr isotopic evidence. *Tectonophysics* 284, 101–133.
- Chen, H.D., Hou, M.C., Xu, X.S., Tian, J.C., 2006. Tectonic evolution and sequence stratigraphic framework in South China during Caledonian. *J. Chengdu Univ. Technol.* 33 (1), 1–8 (in Chinese with English abstract).
- Chen, C.H., Lee, C.Y., Hsieh, P.S., Zeng, W., Zhou, H.W., 2008. Approaching the age problem for some metamorphosed Precambrian basement rocks and Phanerozoic granitic bodies in the Wuyishan area: the application of EMP monazite age dating. *Geol. J. China Univ.* 14 (1), 1–15.
- Chen, J.L., Xu, J.F., Wang, B.D., Kang, Z.Q., Li, J., 2010. Origin of Cenozoic alkaline potassiac volcanic rocks at KonglongXiang, Lhasa terrane, Tibetan Plateau: products of partial melting of a mafic lower-crustal source? *Chem. Geol.* 273, 286–299.
- Chen, J.Y., Yang, J.H., Zhang, J.H., Sun, J.F., Wilde, S.A., 2013. Petrogenesis of the Cretaceous Zhangzhou batholith in southeastern China: zircon U-Pb age and Sr-Nd-Hf-O isotopic evidence. *Lithos* 162–163, 140–156.
- Chu, N.C., Taylor, R.N., Chavagnac, V., Nesbitt, R.W., Boella, R.M., Milton, J.A., Germain, C.R., Bayon, G., Burton, K., 2002. Hf isotope ratio analysis using multicollector inductively coupled plasma mass spectrometry: an evaluation of isobaric interference corrections. *J. Anal. At. Spectrom.* 17, 1567–1574.
- Chu, Y., Faure, M., Lin, W., Wang, Q.C., 2012a. Early Mesozoic tectonics of the South China block: insights from the Xuefengshan intracontinental orogen. *J. Asian Earth Sci.* 61, 199–220.
- Chu, Y., Lin, W., Faure, M., Wang, Q.C., Ji, W.B., 2012b. Phanerozoic tectonothermal events of the Xuefengshan Belt, central South China: implications from U/Pb age and Lu/Hf determinations of granites. *Lithos* 150, 243–255.
- Clemens, J.D., 2003. S-type granitic magmas-petrogenetic issues, models and evidence. *Earth Sci. Rev.* 61, 1–18.
- Collins, W.J., 1996. Lachlan Fold Belt granitoids: products of three-component mixing. *Trans. Roy. Soc. Edinb.: Earth Sci.* 87, 171–181.
- Collins, W.J., 1998. Evaluation of petrogenetic models for Lachlan Fold Belt granitoids: implications for crustal architecture and tectonic models. *Aust. J. Earth Sci.* 45, 483–500.
- De, B.P., Taylor, P.D.P., 1993. Table of the isotopic compositions of the elements. *Int. J. Mass Spectrom.* 123, 149–166.
- Dewey, J.F., 1969. Evolution of the Appalachian/Caledonian orogen. *Nature* 222, 124–129.
- Ducea, M., Saleeby, J., 1998. A case for delamination of the deep batholithic crust beneath the Sierra Nevada, California. *Int. Geol. Rev.* 40, 78–93.

- Elburg, M.A., 1996. Evidence of isotopic equilibration between microgranitoid enclaves and host granodiorite, Warburton granodiorite, Lachlan Fold Belt, Australia. *Lithos* 26, 115–134.
- England, P., Houseman, G., 1989. Extension during continental convergence, with application to the Tibetan Plateau. *J. Geophys. Res.* 94, 17561–17579.
- England, P.C., Thompson, A.B., 1984. Pressure–temperature–time paths of regions metamorphism I. Heat transfer during the evolution of regions of thickened continental crust. *J. Petrol.* 25, 894–928.
- Faure, M., Shu, L.S., Wang, B., Charvet, J., Choulet, F., Monié, P., 2009. Intracontinental subduction: a possible mechanism for the Early Paleozoic Orogen of SE China. *Terra Nova* 21, 360–368.
- Fillerup, M.A., Knapp, J.H., Knapp, C.C., Raileanu, V., 2010. Mantle earthquakes in the absence of subduction? Continental delamination in the Romanian Carpathians. *Lithosphere* 2, 333–340.
- Finger, F., Roberts, M.P., Haunschmid, B., Schermaier, A., Steyrer, H.P., 1997. Variscan granitoids of central Europe: their typology, potential sources and tectonothermal relations. *Mineral. Petrol.* 61, 67–96.
- Gao, T.J., 1991. Two significant terrane boundaries in the southeast coast of China. *Fujian Geol.* 10, 1–15 (in Chinese).
- Garcia, D., Fonteilles, M., Moutte, J., 1994. Sedimentary fractionations between Al, Ti and Zr and the genesis of strongly peraluminous granites. *J. Geol.* 102, 411–422.
- Gray, C.M., 1984. An isotopic mixing model for the origin of granitic rocks in southeastern Australia. *Earth Planet. Sci. Lett.* 70, 47–60.
- Griffin, W.L., Pearson, N.J., Elusiv, E., Jackson, S.E., van Achterberg, E., O'Reilly, S.Y., She, S.R., 2000. The Hf isotope composition of carbonic mantle: LAM-MC-ICPMS analysis of zircon megacrysts in kimberlites. *Geochim. Cosmochim. Acta* 64, 133–147.
- Griffin, W.L., Wang, X., Jackson, S.E., Pearson, N.J., O'Reilly, S.Y., Xu, X.S., Zhou, X.M., 2002. Zircon chemistry and magma mixing, SE China: in-situ analysis of Hf isotopes, Tonglu and Pingtan igneous complexes. *Lithos* 61, 237–269.
- Gromet, L.P., Dymek, R.F., Haskin, L.A., Korotev, R.L., 1984. The “North American shale composite”: its compilation, major and trace element characteristics. *Geochim. Cosmochim. Acta* 48, 2469–2482.
- Gruau, G., Rosing, M., Bridgwater, D., Gill, R.C.O., 1996. Resetting of Sm–Nd systematics during metamorphism of >3.7-Ga rocks: implications for isotopic models of early Earth differentiation. *Chem. Geol.* 133, 225–240.
- Guo, L.Z., Shi, Y.S., Lu, H.F., Ma, R.S., Dong, H.G., Yang, S.F., 1989. The pre-Devonian tectonic patterns and evolution of South China. *J. SE Asian Earth Sci.* 3, 87–93.
- Guo, L.G., Liu, Y.P., Li, C.Y., Xu, W., Ye, L., 2009. SHRIMP zircon U–Pb geochronology and lithogeochemistry of Caledonian granites from the Lajunshan area, southeastern Yunnan province, China: implications for the collision between the Yangtze and Cathaysia blocks. *Geochim. J.* 43, 101–122.
- Gutiérrez-Alonso, G., Murphy, B., Fernández-Suárez, J., Weil, A.B., Franco, M.P., Gonzalo, J.C., 2011. Lithospheric delamination in the core of Pangea: Sm–Nd insights from the Iberian mantle. *Geology* 39, 155–158.
- Gvirtzman, Z., 2002. Partial detachment of a lithospheric root under the southeast Carpathians: toward a better definition of the detachment concept. *Geology* 30, 51–54.
- Healy, B., Collins, W.J., Richards, S.W., 2004. A hybrid origin for Lachlan S-type granites: the Murrambridge Batholith example. *Lithos* 78, 197–216.
- Hsu, K.J., 1994. Tectonic facies in an archipelago model of intra-plate orogenesis. *GSAToday* 4 (12), 289–293.
- Hu, Z.C., Liu, Y.S., Chen, L., Zhou, L., Li, M., Zong, K.Q., Zhu, L.Y., Gao, S., 2011. Contrasting matrix induced elemental fractionation in NIST SRM and rock glasses during laser ablation ICP-MS analysis at high spatial resolution. *J. Anal. At. Spectrom.* 26, 425–430.
- Hua, R.M., Zhang, W.L., Chen, P.R., Zhai, W., Li, G.L., 2013. Relationship between Caledonian granitoids and large-scale mineralization in South China. *Geol. J. China Univ.* 19, 1–11.
- Huang, J.Q., 1978. An outline of the tectonic characteristics of China. *Eclogae Geol. Helv.* 71 (3), 611–635 (in Chinese).
- Huang, X.L., Yu, Y., Li, J., Tong, L.X., Chen, L.L., 2013. Geochronology and petrogenesis of the early Paleozoic I-type granite in the Taishan area, South China: middle-lower crustal melting during orogenic collapse. *Lithos* 177, 268–284.
- Hung, H.K., 2010. Overview of magmatism in northwestern Vietnam. *Ann. Soc. Geol. Pol.* 80, 185–226.
- Jackson, S.E., Pearson, N.J., Griffin, W.L., Belousova, E.A., 2004. The application of laser ablation-inductively coupled plasma-mass spectrometry to in situ U–Pb zircon geochronology. *Chem. Geol.* 211, 47–69.
- Jiménez-Munt, I., Fernández, M., Vergés, J., Platt, J.P., 2008. Lithosphere structure underneath the Tibetan Plateau inferred from elevation, gravity and geoid anomalies. *Earth Planet. Sci. Lett.* 267, 276–289.
- Kemp, A.I.S., Hawkesworth, C.J., Foster, G.L., Paterson, B.A., Woodhead, J.D., Hergt, J.M., Gray, C.M., Whitehouse, M.J., 2007. Magmatic and crustal differentiation history of granitic rocks from Hf–O isotopes in zircon. *Science* 315, 980–983.
- Keskin, M., 2003. Magma generation by slab steepening and breakoff beneath a subduction-accretion complex: an alternative model for collision-related volcanism in Eastern Anatolia, Turkey. *Geophys. Res. Lett.* 30, 8046. <http://dx.doi.org/10.1029/2003GL018019>.
- Knapp, J.H., Knapp, C.C., Raileanu, V., Matenco, L., Mocanu, V., Dinu, C., 2005. Crustal constraints on the origin of mantle seismicity in the Vrancea Zone, Romania: the case for active continental delamination. *Tectonophysics* 410, 311–323.
- Kohút, M., Nabelek, P.I., 2008. Geochemical and isotopic (Sr, Nd and O) constraints on sources of Variscan granites in the Western Carpathians – implications for crustal structure and tectonics. *J. Geosci.* 53, 307–322.
- Krystopowicz, N.J., Currie, C.A., 2013. Crustal eclogitization and lithosphere delamination in orogens. *Earth Planet. Sci. Lett.* 361, 195–207.
- Li, X.H., 1991. Geochronology of the Wanyangshan-Zhuguangshan granitoid batholith: implication for the crust development. *Sci. China: Ser. B* 34, 620–629.
- Li, Z.X., Li, X.H., 2007. Formation of the 1300-km-wide intracontinental orogen and postorogenic magmatic province in Mesozoic South China: a flat-slab subduction model. *Geology* 35, 179–182.
- Li, X.H., McCulloch, M.T., 1996. Nd isotopic evolution of sediments from the southern margin of the Yangtze Block and its tectonic significance. *Acta Petrol. Sinica* 12 (3), 359–369 (in Chinese with English abstract).
- Li, X.H., Tatsumoto, M., Prewo, W.R., 1989. Age and origin of the Tanghu granite, southeast China: results from U–Pb single zircon and Nd isotopes. *Geology* 17, 395–399.
- Li, Z.X., Li, X.H., Zhou, H.W., Kinny, P.D., 2002. Grenvillian continental collision in south China: new SHRIMP U–Pb zircon results and implications for the configuration of Rodinia. *Geology* 30, 163–166.
- Li, X.H., Liu, D.Y., Sun, M., Li, W.X., Liang, X.R., Liu, Y., 2004. Precise Sm–Nd and U–Pb isotopic dating of the super-giant Shizhuoyan polymetallic deposit and its host granite, Southeast China. *Geol. Mag.* 141, 225–231.
- Li, Z.X., Wartho, J.-A., Occhipinti, S., Zhang, C.L., Li, X.H., Wang, J., Bao, C., 2007. Early history of the eastern Sibao orogen (South China) during the assembly of Rodinia: New mica 40Ar/39Ar dating and SHRIMP U–Pb detrital zircon provenance constraints. *Precambr. Res.* 159, 79–94.
- Li, X.H., Li, W.X., Li, Z.X., Lo, C.H., Wang, J., Ye, M.F., Yang, Y.H., 2009. Amalgamation between the Yangtze and Cathaysia Blocks in South China: constraints from SHRIMP U–Pb zircon ages, geochemistry and Nd–Hf isotopes of the Shuangxiu volcanic rocks. *Precambr. Res.* 174, 117–128.
- Li, Z.X., Li, X.H., Wartho, J.A., Clark, C., Li, W.X., Zhang, C.L., Bao, C., 2010. Magmatic and metamorphic events during the early Paleozoic Wuyi–Yunkai orogeny, southeastern South China: new age constraints and pressure–temperature conditions. *Geol. Soc. Am. Bull.* 122, 772–793.
- Li, L.M., Sun, M., Wang, Y.J., Xing, G.F., Zhao, G.C., Cai, K.D., Zhang, Y.Z., 2011. Geochronological and Geochemical study of Palaeoproterozoic gneissic granites and clinopyroxene xenoliths from NW Fujian, SE China: Implications for the crustal evolution of the Cathaysia Block. *J. Asian Earth Sci.* 41, 204–212.
- Li, Z., Qiu, J.S., Yang, X.M., 2014. A review of the geochronology and geochemistry of Late Yanshanian (Cretaceous) plutons along the Fujian coastal area of southeastern China: Implications for magma evolution related to slab break-off and rollback in the Cretaceous. *Earth Sci. Rev.* 128, 232–248.
- Liu, R., Zhang, L., Zhou, H.W., Zhong, Z.Q., Zeng, W., Xiang, H., Ji, S., Lv, X.Q., Li, C.Z., 2008. Petrogenesis of the Caledonian migmatites and related granites in northwestern Fujian Province, South China: syndeformational crustal anatexis. *Acta Petrol. Sinica* 24, 1205–1222.
- Liu, Y.S., Gao, S., Hu, Z.C., Gao, C.G., Zong, K.Q., Wang, D.B., 2010a. Continental and oceanic crust recycling-induced melt–peridotite interactions in the Trans-North China Orogen: U–Pb dating, Hf isotopes and trace elements in zircons from mantle xenoliths. *J. Petrol.* 51, 537–571.
- Liu, Y.S., Hu, Z.C., Zong, K.Q., Zong, K.Q., Gao, S., Xu, J., Chen, H.H., 2010b. Reappraisal and refinement of zircon U–Pb isotope and trace element analyses by LA-ICP-MS. *Chin. Sci. Bull.* 55 (15), 1535–1546.
- Liu, L., Qiu, J.S., Li, Z., 2013. Origin of mafic microgranular enclaves (MMEs) and their host quartz monzonites from the Muchen pluton in Zhejiang Province, Southeast China: implications for magma mixing and crust–mantle interaction. *Lithos* 160–161, 145–163.
- Ludwig, K.R., 2003. User's Manual for Isoplot 3.00 a Geochronological Toolkit for Microsoft Excel.
- Mass, R., Nicholls, I.A., Legg, C., 1997. Igneous and metamorphic enclaves in the S-type Dedick granodiorite: geochemical and Nd–Sr isotopic evidence for crustal melting and magma mixing. *J. Petrol.* 38, 815–841.
- McLellan, J.M., Selleck, B.W., Hamilton, M.A., Bickford, M.E., 2010. Late- to post-tectonic setting of some major Proterozoic anorthosite–mangerite–charnockite–granite AMCG suites. *Can. Mineral.* 48, 1025–1046.
- Miller, C.F., 1985. Are strongly peraluminous magmas derived from pelitic sedimentary sources? *J. Geol.* 93, 673–689.
- Nabelek, P.I., Liu, M., 1999. Leucogranites in the Black Hills of South Dakota: the consequence of shear heating during continental collision. *Geology* 27, 523–526.
- Allen, C.M., Williams, I.S., Stephens, C.J., Fielding, C.R., 1998. Granite genesis and basin formation in an extensional setting: the magmatic history of the northernmost New England Orogen. *Aust. J. Earth Sci.* 45, 875–888.
- Patiño Douce, A.E., 1995. Experimental generation of hybrid silicic melts by reaction of high-Al basalt with metamorphic rocks. *J. Geophys. Res.* 100, 15623–15639.
- Patiño Douce, A.E., Harris, N., 1998. Experimental constraints on Himalayan anatexis. *J. Petrol.* 39, 689–710.
- Perry, F.V., Baldridge, W.S., DePaolo, D.J., 1988. Chemical and isotopic evidence for lithospheric thinning beneath the Rio Grande rift. *Nature* 332, 432–434.
- Petford, N., Atherton, M., 1996. Na-rich partial melts from newly underplated basaltic crust: the Cordillera Blanca Batholith, Peru. *J. Petrol.* 37, 1491–1521.
- Phillips, G., Landenberger, B., Belousova, E.A., 2011. Building the New England Batholith, eastern Australia—linking granite petrogenesis with geodynamic setting using Hf isotopes in zircon. *Lithos* 122, 1–12.
- Platt, J.P., England, P.C., 1994. Convective removal of lithosphere beneath mountain belts: thermal and mechanical consequences. *Am. J. Sci.* 294, 307–336.
- Qi, L., Hu, J., Gregoire, D.C., 2000. Determination of trace elements in granites by inductively coupled plasma-mass spectrometry. *Talanta* 51, 507–513.
- Qiu, Y.M., Gao, S., McNaughton, N.J., Groves, D.J., Ling, W.L., 2000. First evidence of >3.2 Ga continental crust in the Yangtze craton of South China and its

- implications for Archean crustal evolution and Phanerozoic tectonics. *Geology* 28, 11–14.
- Qiu, J.S., Xiao, E., Hu, J., Xu, X.S., Jiang, S.Y., Li, Z., 2008. Petrogenesis of highly fractionated I-type granites in the coastal area of northeastern Fujian Province. Constraints from zircon U-Pb geochronology, geochemistry and Nd-Hf isotopes. *Acta Petrol. Sinica* 24, 2468–2484 (in Chinese, with English abstract).
- Ren, J., 1991. On the geotectonics of southern China. *Acta Geol. Sinica—English Ed.* 4 (2), 111–130.
- Roger, F., Leloup, P.H., Jolivet, M., Lacassin, R., Trinh, P.T., Brunel, M., Seward, D., 2000. Long and complex thermal history of the Song Chay metamorphic dome (Northern Vietnam) by multi-system geochronology. *Tectonophysics* 321, 449–466.
- Rossi, J.N., Toselli, A.J., Saavedra, J., Sial, A.N., Pellitero, E., Ferreira, V.P., 2002. Common crustal sources for contrasting peraluminous facies in the early Paleozoic Capillitas Batholith, NW Argentina. *Gondwana Res.* 5, 325–337.
- Sandeman, H.A., Clarke, A.H., 2003. Glass-rich, cordierite-biotite Rhyodacite, Valle Ninhuisa, Puno, SE Peru: petrological evidence for hybridisation of 'Lachlan S-type' and potassic mafic magmas. *J. Petrol.* 44, 355–385.
- Scherer, E., Munker, C., Mezger, K., 2001. Calibration of the lutetium–hafnium clock. *Science* 293, 683–687.
- Searle, M.P., Parrish, R.R., Hodges, K.V., Hurford, A., Ayres, M.W., Whitehouse, M.J., 1997. Shisha Pangma leucogranite, south Tibetan Himalaya: field relations, geochemistry, age, origin, and emplacement. *J. Geol.* 105, 295–317.
- Şengör, A.M.C., Özener, S., Genç, T., Zor, E., 2003. East Anatolian high plateau as a mantle-supported, north-south shortened domal structure. *Geophys. Res. Lett.* 30, 8045, 10.1029/2003GL017858.
- Shen, W.Z., Zhu, J.C., Liu, C.S., Xu, S.J., Ling, H.F., 1993. Sm-Nd isotopic study of basement metamorphic rocks in south China and its constraint on material sources of granitoids. *Acta Petrol. Sinica* 9, 115–124 (in Chinese with English abstract).
- Shen, W.Z., Zhang, F.R., Shu, L.S., Wang, L.J., Xiang, L., 2008. Formation age, geochemical characteristics of the Ninggang granite body in Jiangxi Province and its tectonic significance. *Acta Petrol. Sinica* 24 (10), 2244–2254 (in Chinese with English abstract).
- Shen, W.Z., Ling, H.F., Shu, L.S., Zhang, F.R., Xiang, L., 2009. Sm-Nd isotopic compositions of Cambrian–Ordovician strata at the Jinggangshan area in Jiangxi Province. Tectonic implications. *Chin. Sci. Bull.* 54 (10), 1750–1758.
- Slama, J., Kosler, J., Condon, D.J., Crowley, J.L., Gerdes, A., Hanchar, J.M., Horstwood, M.S.A., Morris, G.A., Nasdala, L., Norberg, N., Schaltegger, U., Schoene, N., Tubrett, M.N., Whitehouse, M.J., 2008. Plesovice zircon – a new natural reference material for U-Pb and Hf isotopic microanalysis. *Chem. Geol.* 249, 1–35.
- Steiger, R.H., Jäger, E., 1997. Subcommission on geochronology: convection or the use of decay constants in geo- and cosmo-chronology. *Earth Planet. Sci. Lett.* 36, 359–362.
- Stevens, G., Clemens, J.D., 1993. Fluid-absent melting and the role of fluids in the lithosphere: a slanted summary? *Chem. Geol.* 108, 1–17.
- Streckeisen, A., 1967. Classification and nomenclature of igneous rocks. Final report of an inquiry. *Neues JB Miner. Abh.* 107, 144–204.
- Sun, T., 2006. A new showing the distribution of granites in South China and its explanatory notes. *Geol. Bull. China* 25 (3), 332–335 (in Chinese with English abstract).
- Sun, S.S., McDonough, W.F., 1989. Chemical and isotopic systematics of oceanic basalts: implications for mantle composition and processes. In: Saunders, A.D., Norry, M.J. (Eds.), *Magma in the Ocean Basins*. Geological Society, London, Special Publications, vol. 42, pp. 313–345.
- Sylvester, P.J., 1998. Postcollisional strongly peraluminous granites. *Lithos* 45, 29–44.
- Tang, M., Wang, X.L., Shu, X.J., Wang, D., Yang, T., Gopon, G., 2014. Hafnium isotopic heterogeneity in zircons from granitic rocks: geochemical evaluation and modeling of "zircon effect" in crustal anatexis. *Earth Planet. Sci. Lett.* 389, 188–199.
- Taylor, S.R., McLennan, S.M., 1985. *The Continental Crust: Its Composition and Evolution*. Blackwell, Oxford Press, 312p.
- Thompson, A.B., Connolly, J.A.D., 1995. Melting of the continental crust: some thermal and petrological constraints on anatexis in continental collision zones and other tectonic settings. *J. Geophys. Res.* 100 (B8), 15565–15579.
- Ting, W.K., 1929. The orogenic movement in China. *Geol. Soc. China* 8 (1), 151–170 (in Chinese with English abstract).
- Turner, S., Sandiford, M., Foden, J., 1992. Some geodynamic and compositional constraints on "postorogenic" magmatism. *Geology* 20, 931–934.
- Vernon, R.H., Etheridge, M.A., Wall, V.J., 1988. Shape and microstructure of microgranitoid enclaves: indicators of magma mingling and flow. *Lithos* 22, 1–11.
- Vervoort, J.D., Blighert-Toft, J., 1999. Evolution of the depleted mantle; Hf isotope evidence from juvenile rocks through time. *Geochim. Cosmochim. Acta* 63, 533–556.
- Villaros, A., Stevens, G., Moyen, J.F., Buick, I.S., 2009. The trace element compositions of S-type granites: evidence for disequilibrium melting and accessory phase entrainment in the source. *Contrib. Miner. Petrol.* 158, 543–561.
- Villaseca, C., Barbero, L., Herreros, V., 1998a. A re-examination of the typology of peraluminous granite types in intracontinental orogenic belts. *Trans. Roy. Soc. Edinb.: Earth Sci.* 89, 113–119.
- Villaseca, C., Barbero, L., Rogers, G., 1998b. Crustal origin of Hercynian peraluminous granitic batholiths of central Spain: petrological, geochemical and isotopic (Sr, Nd) constraints. *Lithos* 43, 55–79.
- Waight, T.E., Mass, R., Nicholls, I.A., 2001. Geochemical investigations of microgranitoid enclaves in the S-type Cowra Granodiorite, Lachlan Fold Belt, SE Australia. *Lithos* 56, 165–186.
- Wan, Y., Liu, D., Wilde, S.A., Cao, J., Chen, B., Dong, C., Song, B., Du, L., 2010. Evolution of the Yunkai Terrane, South China: evidence from SHRIMP zircon U-Pb dating, geochemistry and Nd isotope. *J. Asian Earth Sci.* 37, 140–153.
- Wang, D.Z., 2004. The study of granitic rocks in South China: looking back and forward. *Geol. J. China Univ.* 10, 305–314 (in Chinese with English abstract).
- Wang, J., Sun, D., Chang, X., Deng, S., Zhang, H., Zhou, H., 1998. U-Pb dating of the Napeng granite at the NW margin of the Yunkai block, Guangdong, South China. *Acta Mineral. Sinica* 18, 130–133 (in Chinese with English abstract).
- Wang, Y.J., Fan, W.M., Guo, F., Peng, T.P., Li, C.W., 2003. Geochemistry of Mesozoic mafic rocks around the Chenzhou-Linwu fault in South China: implication for the lithospheric boundary between the Yangtze and the Cathaysia Blocks. *Int. Geol. Rev.* 45, 263–286.
- Wang, Q., Xu, J.F., Jian, P., Bao, Z.W., Zhao, Z.H., Li, C.F., Xiong, X.L., Ma, J.L., 2006a. Petrogenesis of adakitic porphyries in an extensional tectonic settings in Dexing, South China: implications for the genesis of porphyry copper mineralization. *J. Petrol.* 47, 119–144.
- Wang, X.L., Zhou, J.C., Qiu, J.S., Zhang, W.L., Liu, X.M., Zhang, G.L., 2006b. LA-ICP-MS U-Pb zircon geochronology of the Neoproterozoic igneous rocks from Northern Guangxi, South China: implications for tectonic evolution. *Precambr. Res.* 145, 111–130.
- Wang, Y.J., Fan, W.M., Zhao, G.C., Ji, S.C., Peng, T.P., 2007. Zircon U-Pb geochronology of gneissic rocks in the Yunkai massif and its implication on the Caledonian event in the South China Block. *Gondwana Res.* 12, 404–416.
- Wang, Y.J., Fan, W.M., Cawood, P.A., Li, S.Z., 2008. Sr-Nd-Pb isotopic constraints on multiple mantle domains for Mesozoic mafic rocks beneath the South China Block hinterland. *Lithos* 106, 297–308.
- Wang, Y.J., Zhang, A.M., Fan, W.M., Zhao, G.C., Zang, G.W., Zhang, Y.Z., Zhang, F.F., Li, S.Z., 2011. Kwangian crustal anatexis within the eastern South China Block: Geochemical, zircon U-Pb geochronological and Hf isotopic fingerprints from the gneissoid granites of Wugong and Wuyi-Yunkai Domains. *Lithos* 127, 239–260.
- Wang, Y.J., Wu, C.M., Zhang, A.M., Fan, W.M., Zhang, Y.H., Zhang, Y.Z., Peng, T.P., Yin, C.Q., 2012. Kwangian and Indosian reworking of the eastern South China Block: constraints on zircon U-Pb geochronology and metamorphism of amphibolites and granulites. *Lithos* 150, 227–242.
- Wang, X.L., Zhou, J.C., Wan, Y.S., Kitajima, K., Wang, D., Qiu, J.S., Sun, T., 2013a. Magmatic evolution and Crustal recycling for Neoproterozoic strongly peraluminous granitoids from southern China: Hf and O isotopes in zircon. *Earth Planet. Sci. Lett.* 366, 71–82.
- Wang, Y.J., Fan, W.M., Zhang, G.W., Zhang, Y.H., 2013b. Phanerozoic tectonics of the South China Block: key observations and controversies. *Gondwana Res.* 23, 1273–1305.
- Wang, Y.J., Zhang, A.M., Fan, W.M., Zhang, Y.H., Zhang, Y.Z., 2013c. Origin of paleosubduction-modified mantle for Silurian gabbro in the Cathaysia Block: Geochronological and geochemical evidence. *Lithos* 160, 37–54.
- Wang, D., Zheng, J.P., Ma, Q., Griffin, W.L., Zhao, H., Wong, J., 2013d. Early Paleozoic crustal anatexis in the intraplate Wuyi-Yunkai orogen, South China. *Lithos* 175–176, 124–145.
- Wiedenbeck, M., Allé, P., Corfu, F., Griffin, W.L., Meier, M., Oberli, F., von Quadt, A., Roddick, J.C., Spiegel, W., 1995. Three natural zircon standards for U-Th-Pb, Lu-Hf, trace element and REE analyses. *Geostandards Newslett.* 19, 1–23.
- Winchester, J.A., Floyd, P.A., 1977. Geochemical discrimination of different magma series and their differentiation products using immobile elements. *Chem. Geol.* 20, 325–343.
- Wolf, M.B., London, D., 1994. Apatite dissolution into peraluminous haplogranitic melts: an experimental study of solubilities and mechanisms. *Geochim. Cosmochim. Acta* 58, 4127–4145.
- Wu, F.Y., Jahn, B.M., Wilde, S.A., Lo, C.H., Yui, T.F., Lin, Q., Ge, W.C., Sun, D.Y., 2003. Highly fractionated I-type granites in NE China (II): isotopic geochemistry and implications for crustal growth in the Phanerozoic. *Lithos* 67, 191–204.
- Wu, F.Y., Li, X.H., Yang, J.H., Zheng, Y.F., 2007. Discussions on the petrogenesis of granites. *Acta Petrol. Sinica* 23, 1217–1238 (in Chinese with English abstract).
- Xia, X.P., Sun, M., Zhao, G.C., Wang, Y.J., 2011. Quasi-simultaneous determination of U-Pb and Hf isotope compositions of zircon by excimer laser-ablation multiple-collector ICPMS. *J. Anal. At. Spectrom.* 26, 1868–1871.
- Xia, Y., Xu, X.S., Zou, H.B., Liu, L., 2014. Early Paleozoic crust–mantle interaction and lithosphere delamination in South China Block: evidence from geochronology, geochemistry, and Sr-Nd-Hf isotopes of granites. *Lithos* 184–187, 416–435.
- Xu, X.S., O'Reilly, S.Y., Griffin, W.L., Deng, P., Pearson, N.J., 2005. Relict Proterozoic basement in the Nanling Mountains (SE China) and its tectonothermal overprinting. *Tectonics* 24, 1–16.
- Yan, D.P., Zhou, M.F., Wang, C.Y., Xia, B., 2006. Structural and geochronological constraints on the tectonic evolution of the Dulong-Song Chay tectonic dome in Yunnan province, SW China. *J. Asian Earth Sci.* 28, 332–353.
- Yao, W.H., Li, Z.X., Li, W.X., Wang, X.C., Li, X.H., Yang, J.H., 2012. Post-kinematic lithospheric delamination of the Wuyi-Yunkai orogen in South China: evidence from ca. 435 Ma high-Mg basalts. *Lithos* 154, 115–129.
- YNBGM (Bureau of Geology and Mineral Resources of Yunnan Province), 1976. Geological map of the Yunnan Province. Sheet F-49-XVII (Maguan) scale 1: 200,000.
- YNBGM (Bureau of Geology and Mineral Resources of Yunnan Province), 1990. Regional Geology of the Yunnan Province. Geological Publishing House, Beijing, pp. 1–729 (in Chinese with English abstract).

- Yu, J.H., O'Reilly, S.Y., Wang, L.J., Griffin, W.L., Zhang, M., Wang, R.C., Jiang, S.Y., Shu, L.S., 2008. Where was South China in the Rodinia supercontinent? Evidence from U-Pb geochronology and Hf isotopes of detrital zircons. *Precambr. Res.* 164, 1–15.
- Zen, E., 1986. Aluminum enrichment in silicate melts by fractional crystallization: some mineralogic and petrographic constraints. *J. Petrol.* 27, 1095–1117.
- Zhang, H.F., Parrish, R., Zhang, L., Xu, W.C., Yuan, H.L., Gao, S., Crowley, Q.G., 2007. A-type granite and adakitic magmatism association in Songpan-Garzê fold belt, eastern Tibetan Plateau: implication for lithospheric delamination. *Lithos* 97, 323–335.
- Zhang, A.M., Wang, Y.J., Fan, W.M., Zhang, F.F., Zhang, Y.Z., 2011. LA-ICPMS zircons U-Pb geochronology and Hf isotopic composition of the Taoxi migmatite (Wuping): constrains on the formation age of the Taoxi complex and the Yu'nan event. *Geotecton. Metall.* 35, 64–72.
- Zhang, A.M., Wang, Y.J., Fan, W.M., Zhang, Y.Z., Yang, J., 2012a. Earliest Neoproterozoic (ca. 1.0 Ga) arc-back-arc basin nature along the northern Yunkai Domain of the Cathaysia Block: geochronological and geochemical evidence from the metabasite. *Precambr. Res.* 220–221, 217–233.
- Zhang, F.F., Wang, Y.J., Zhang, A.M., Fan, W.M., Zhang, Y.Z., Zi, J.W., 2012b. Geochronological and geochemical constraints on the petrogenesis of Middle Paleozoic (Kwangssian) massive granites in the eastern South China Block. *Lithos* 150, 188–208.
- Zhao, G.C., Cawood, P.A., 1999. Tectonothermal evolution of the Mayuan assemblage in the Cathaysia Block: new evidence for Neoproterozoic collisional-related assembly of the South China craton. *Am. J. Sci.* 299, 309–339.
- Zhao, G.C., Cawood, P.A., 2012. Precambrian geology of China. *Precambr. Res.* 222–223, 13–54.
- Zhao, K.D., Jiang, S.Y., Sun, T., Chen, W.F., Ling, H.F., Chen, P.R., 2013. Zircon U-Pb dating, trace element and Sr-Nd-Hf isotope geochemistry of Paleozoic granites in the Miao'ershan–Yuechengling batholith, South China: implication for petrogenesis and tectonic–magmatic evolution. *J. Asian Earth Sci.* 74, 244–264.
- Zheng, Y.F., Zhang, S.B., Zhao, Z.F., Wu, Y.B., Li, X.H., Li, Z.X., Wu, F.Y., 2007. Contrasting zircon Hf and O isotopes in the two episodes of Neoproterozoic granitoids in South China: implications for growth and reworking of continental crust. *Lithos* 96, 127–150.